DIELECTRIC CHARACTERISTICS OF PZT 95/5
FERROELECTRIC CERAMICS AT HIGH PRESSURES

By

RICHARD KENT SPEARS

A DISSERTATION PRESENTED TO THE GRADUATE COUNCIL
OF THE UNIVERSITY OF FLORIDA
IN PARTIAL FULFILLMENT OF THE REQUIREMENTS FOR THE
DEGREE OF DOCTOR OF PHILOSOPHY

UNIVERSITY OF FLORIDA

1977

This dissertation is dedicated to my father,

Lawrence E. Spears

ACKNOWLEDGEMENTS

for their advice concerning shock depolarization dielectric requirements.

Gratitude is expressed to the General Electric Company, Neutron Devices Department, St. Petersburg, Florida, for its assistance in this project. The effort extended by Mr. J. R. Novak and Mr. F. H. McNabb of the General Electric second shift maintenance crew for their role in rebuilding the press is greatly appreciated. Thanks are extended to Mr. J. L. Pethe for his effort in constructing the low voltage looper which was built solely for this program.

Finally, as a husband and father, it is difficult to put into words the deep appreciation that needs to be extended to some very important people in my life, my family--Evelyn, Michael, Steven, Lawrence, Lori, and Amy--who have put up with the general turmoil that my graduate studies have created over the past few years.

TABLE OF CONTENTS

Abstract of Dissertation Presented to the Graduate Council
of the University of Florida in Partial Fulfillment of the
Requirements for the Degree of Doctor of Philosophy

DIELECTRIC CHARACTERISTICS OF PZT 95/5
FERROELECTRIC CERAMICS AT HIGH PRESSURES

By

Richard Kent Spears

August, 1977

Chairman: Edward K. Walsh
Major Department: Engineering Sciences

The room temperature dielectric properties of a

ferroelectric ceramic having a nominal composition of 95

atomic % lead zirconate and 5 atomic % lead titanate

(called PZT 95/5) with a niobium dopant was examined at

high hydrostatic pressures using a tetrahedral anvil apparatus.

This ceramic has practical applications as a power source

in which large quantities of charge are released by

dynamic (shock wave) depolarization. Numerous mathematical

models of this process have been proposed; however, the

use of models has been limited because of the lack of

high pressure electrical properties. This study attempted

to provide these data on PZT 95/5 by determining the small

signal and high electric field dielectric properties at

pressures over 4 GPa.

A stainless steel test cell was fabricated which contained the manganin gage, the sample, and the insulating fluid (1 to 1 mixture of isopentane and n-pentane). Polyethylene plugs held the fluid in place and one plug contained holes having #28 magnet wire lead wire which was capable of supplying 2000 volts to the specimen.

Pressure depolarization of PZT 95/5 is attributed to the inducement of the 0.4 GPa nonpolar antiferroelectric phase; thus, bound ferroelectric charge is released at the transition.

Experimental shock propagation studies on PZT 95/5 have resulted in a two and sometimes three wave structure. There has been some indication of additional high pressure phases. An additional objective was to detect high pressure phase changes using dielectric measurements.

When the dielectric constant was plotted versus pressure, there was a gradual increase up to the ferroelectric-antiferroelectric transition. The dielectric constant then fell and gradually leveled off. At approximately 2 GPa, a dielectric discontinuity was observed on every test. This was initially attributed to a phase change; however, due to the fact that it was irreversible and that the specimen was extremely fragile, the cause was attributed to the collapse of pores in the ceramic.

Hysteresis loops were run on specimens up to the transition. It was found that the antiferroelectric state

could be induced at a lower pressure than had been measured
using small signal means by continued looping at an inter-
mediate pressure. This value is probably a truer transi-
tion than the small signal value which is apparently measur-
ing a metastable ferroelectric state.

When a sample was retested at zero psi after it
had been pressure depolarized, only 180° domain realignment
was evident as opposed to 180° and 90° on thermally depoled
samples. This as well as other dielectric data indicate
that the metastable antiferroelectric phase may remain at
zero pressure if an electric field is not applied.

As has been performed with other ferroelectric
materials in the nonpolar paraelectric state, it was pos-
sible to fit small signal data at pressures immediately
greater than the ferroelectric-antiferroelectric transi-
tion in the antiferroelectric state to a Curie-Weiss-like
relationship--$\varepsilon = C*/(p-p_0)$. However, a two termed equa-
tion rather than one was needed. The second term con-
sisted of the y intercept.

These results could be applied directly to some
of the simplified shock depolarization models. However,
current theories make use of electric relaxation proper-
ties. An examination consisting of plotting the complex
dielectric modulus components revealed that to use these
data effectively, high frequency measurements would be
required.

CHAPTER 1

INTRODUCTION

The objective of this study was to experimentally determine the static high pressure dielectric characteristics of a niobium doped 95% lead zirconate – 5% lead titanate ferroelectric ceramic.* These data can be applied to mathematical models depicting the depolarization of ferroelectric ceramics in an intense high pressure (shock) environment. Since the investigation involved the application of strong electric fields to minute samples at high pressures, new experimental techniques had to be developed.

Although ferroelectric materials are most commonly used as acoustic transducers, the present study concerns a unique application reported by Nielson (1) in 1956 termed shock depolarization. Nielson indicated that large quantities of charge could be released by stressing the ferroelectric with a shock wave having an intensity above a certain threshold pressure.

---

*All compositional percentages in this study are in atomic percent unless otherwise stated.

An important ferroelectric material used in shock depolarization applications is a niobium doped ceramic composed of 95% lead zirconate and 5% lead titanate commonly known as PZT 95/5. On the lead zirconate-lead titanate composition-temperature phase diagram, a ferroelectric (FE) phase near the PZT 95/5 composition is adjacent to an antiferroelectric (AFE) phase. For PZT 95/5, depolarization is brought about by the pressure inducement of the first-order FE-AFE polymorphic phase change. Under isostatic pressure, this transition occurs at 0.25 to 0.5 GPa, which is considerably below the pressure usually applied during shock depolarization. For undoped PZT 95/5, the composition-temperature phase diagram, although basically straightforward, becomes complex near the Curie temperature (227° C) where another AFE phase is in close proximity (2, 3). During shock depolarization, where there is an adiabatic temperature increase at the shock front, it is possible that both AFE phases along with the paraelectric phase would be encountered.

The characterization of materials such as PZT 95/5, which contain four to five major elements along with dopants and impurities, is difficult because of inhomogeneities and density variations. Further, the electrical response is influenced by variations in grain size, void size, and/or material phase changes. As an electrical circuit component, the shocked ferroelectric exhibits an

electrical impedance that varies with pressure and time.
Modeling of this process has been examined by Anderson
(4), Lysne and Percival (5), Chen and McCarthy (6), and
others.   Recent work (7) has been carried out on a shock
depolarization model that will depict the electrical
response of PZT 95/5 when shocked up to 3.5 GPa.   An ade-
quate description of the high pressure properties of this
material was available with the exception of permittivity.
Due to the difficulty in determining this property dynam-
ically, it has been proposed that static measurements be
made and adapted to the dynamic mode.   This constitutes
the basis for the present study.

In this program only the ambient temperature static
pressure field was investigated.   It is believed that
these data will suffice for a first-order approximation
of the dielectric-pressure response and the corresponding
temperature behavior will be left for future researchers.

A tetrahedral anvil apparatus belonging to the
Materials Science Department was used to obtain the high
static pressures required for these studies.   This unit
had not been in operation at the University of Florida
prior to these tests; thus, this study constituted the
first to be performed using the press.   Operating instruc-
tions are included in Appendix A for future experiments.

Prior to the initiation of the study it was felt
that the ultimate pressures desired were 2.5 to 3.0 GPa.

On two occasions the upper end of the Heise gage was approached to examine the capability of the unit (the second time resulted in a broken anvil). However, the ultimate pressure recorded by the internal manganin cell barely exceeded 4.5 GPa, whereas it was hoped that 6-7 GPa could have been attained. Attempts at improving pressure transmission were not performed since the lower pressures were suitable.

A relative dielectric constant based on small signal measurements as well as on high voltage poling measurements was determined as a function of pressure. These data have direct application to simpler shock depolarization models where average values in the shocked and unshocked regions are sufficient. More refined models require dielectric relaxation parameters which consist chiefly of the instantaneous and static dielectric constant with frequency dependent data in between. The measuring frequencies were limited to below 1 MHz. This appeared to be sufficient to determine the static dielectric constant, but instantaneous values were not determined because of the large interpolation error. Thus, it is recommended that further dielectric examinations be made at higher frequencies.

Other items of interest were found which may not have a direct application to depolarization models but broaden the understanding of the depolarization process

and dielectric characteristics of PZT 95/5. Prior to the
0.32 GPa. FE-AFE transition, the material state (although
predominantly FE) appears to be mixed FE and AFE. High
voltage looping provided the activation energy necessary
to partially stabilize and induce a portion of the AFE
phase. It was possible to induce the entire AFE phase
by continued looping at a pressure approximately 0.11 GPa
lower than when not looped. Thus, it is paradoxical that
an electric field causes the material to favor the FE
state but induces the AFE state.

From an analysis of data on a single sample, it
was found that the dielectric constant immediately after
the transition follows a Curie-Weiss-like relationship
similar to that found in other ferroelectrics in the
nonpolar paraelectric state.

A discontinuity in the dielectric behavior was
detected on all samples at about 2.2 GPa. Initially this
was believed to be a phase change, but since then it has
been attributed to pore collapse in the ceramic.

CHAPTER 2

BACKGROUND

2.1 Properties of Dielectrics

When a dielectric is inserted between two parallel plate electrodes, whose capacitance in air is C_0, the capacitance C is increased by $\varepsilon_s/\varepsilon_0$ or K where ε_s is the permittivity or static dielectric constant, ε_0 is the permittivity of free space ($8.85 \times 10^{-12} n^{-1} \cdot coul^2 \cdot m^{-2}$) and K is the relative dielectric constant. If the charge Q is maintained constant, then the voltage V across the capacitor is reduced (i.e., $V = Q/C = Q/KC_0$) with the dielectric inserted. The fraction of the charge contributing to the voltage increase (Q/K) is called the free charge while the remainder (Q - Q/K) is called the bound charge.

If charge displacement has occurred in a dielectric, it is said to be polarized and the atoms or molecules within the dielectric are said to possess an induced dipole moment whose magnitude depends on the charge and displacement. The dipole moment per unit volume at a point is called the electric polarization $\vec{P}$. In reference to induced charges on surfaces perpendicular to the polar

direction, polarization can also be thought of as charge per unit area.

Polarization is a field vector representing the bound charge density in the dielectric while another field vector, called the electric flux density $\vec{D}$ or dielectric displacement, represents the total charge across the dielectric (i.e., both the bound charge and the free charge). For two parallel plates in a vacuum $\vec{D} = \vec{E}$ (where $\vec{E}$ is the electric field intensity) but with a dielectric inserted, the following results:

$$\vec{D} = \varepsilon_s \vec{E}. \tag{2.1.1}$$

The dependence of polarization on electric field and flux density is as follows:

$$\vec{P} = \vec{D} - \varepsilon_0 \vec{E} = (\varepsilon_s - \varepsilon_0) \vec{E} = \chi \varepsilon_0 \vec{E} \tag{2.1.2}$$

where χ, the dielectric susceptibility, is the ratio of the bound charge density to the free charge density. Susceptibility is formally defined as $\partial\vec{P}/\partial\vec{E}\varepsilon_0$, while the relative dielectric constant is $\partial\vec{D}/\partial\vec{E}$. In terms of susceptibility the relative dielectric constant is

$$K = \chi + 1. \tag{2.1.3}$$

For a dielectric in an alternating field both $\vec{P}$ and $\vec{D}$ vary periodically with time but generally lag behind $\vec{E}$ so that in complex notation if

$$\vec{E}^* = \vec{E}_0 \exp (i\ \omega t) \qquad\qquad (2.1.4)$$

then

$$\vec{D}^* = \vec{D}_0 \exp [i(\omega t - \delta)] \qquad\qquad (2.1.5)$$

where ω is the angular frequency and δ is the phase differ-ence. From Equation 2.1.1, it follows that a complex dielectric constant relates $\vec{D}^*$ and $\vec{E}^*$, i.e.,

$$\vec{D}^* = \varepsilon^* \vec{E}^* \qquad\qquad (2.1.6)$$

and

$$\vec{D}^* = \vec{D}_0 \vec{E}_0^{-1} \exp (-i\delta) = \varepsilon_S(\cos \delta - i \sin \delta).$$
$$\qquad\qquad (2.1.7)$$

It is seen that the ratio $\vec{D}_0 \vec{E}_0^{-1}$ is frequency dependent with two frequency dependent dielectric constants $\vec{D}_0 \vec{E}_0^{-1} \sin \delta$ and $\vec{D}_0 \vec{E}_0^{-1} \cos \delta$ (the dielectric constant is also temperature dependent). These are generally expressed using the single complex dielectric constant as follows:

$$\epsilon^* = \vec{D}_0 \, \vec{E}_0^{-1} \cos \delta - i \, \vec{D}_0 \, \vec{E}_0^{-1} \sin \delta = \epsilon' - i \, \epsilon''.$$

$$(2.1.8)$$

In this equation ϵ' is called the dielectric constant, while ϵ'' is the loss factor. It can be shown that the heat dissipated in a dielectric is proportional to ϵ''. It is seen that the ratio (ϵ''/ϵ') equals tan δ; this is called the dissipation factor and if the dielectric constant (ϵ') and dissipation factor are known, then the loss factor ϵ'' can be determined (i.e., $\epsilon'' = \epsilon'$ tan δ).

In a time varying, dynamic electric field, the response of dielectrics can be treated in a manner similar to the response of other materials under dynamic conditions, i.e., if a field is suddenly applied to a dielectric, the static dielectric constant will not be attained immediately due to the inertia of polarization, but will increase gradually to ϵ_s after it has attained an instantaneous value denoted by ϵ_i. The latter follows the electric field immediately and is called the instantaneous or optical dielectric constant (this is the dielectric constant at infinite frequency).

A well-established relaxation model proposed by Debye which makes use of the Principle of Superposition and the fact that polarization can be described by an exponential law of the form $\exp(-t/\tau)$ with a single relaxation

time (τ) has gained wide acceptance because Debye was able
to show how the results could be applied to a simple molecu-
lar model. By a straightforward derivation (8, p. 91),
relationships known as the Debye equations were obtained
which expressed the complex dielectric constant in terms
of ϵ_s, ϵ_i, ω and τ. These equations are as follows:

$$\epsilon^* = \epsilon_i + (\epsilon_s - \epsilon_i)(1 + i\omega\tau)^{-1} \qquad (2.1.9)$$

$$\epsilon' = \epsilon_i + (\epsilon_s - \epsilon_i)(1 + \omega^2\tau^2)^{-1} \qquad (2.1.10)$$

$$\epsilon'' = (\epsilon_s - \epsilon_i)(\omega\tau)(1 + \omega^2\tau^2)^{-1} \ . \qquad (2.1.11)$$

Experimentally, as a periodic field is applied to
a dielectric, the capacitance and dissipation factor are
the usual parameters which are measured as a function of
frequency. A method of representing and analyzing these
data which is attributed to Cole and Cole (8, p. 93) is
based on plotting the real and imaginary part of the com-
plex dielectric constant in the complex plane (ϵ' vs. ϵ'').
Each point then represents one frequency measurement and
the locus is a semicircle (for a single relaxation time) as
ω varies from 0 to ∞ with its ends intersecting the real
axis at ϵ_i and ϵ_s. For experimental data which cover the
in-between regions of absorption and dispersion, the Cole-
Cole plot constitutes a method for determining ϵ_i and ϵ_s

by extrapolation. For a model representing a distribution of relaxation times the locus is still circular in shape with a chord of the circle lying on the real axis having ε_i and ε_s at the extremities of the chord (8, p. 93).

The relationship between polarization and electric field is one of the most distinguishing characteristics of ferroelectrics. By using a simple circuit devised by Sawyer and Tower (9), $\vec{P}$ and $\vec{E}$ can be displayed directly on the coordinates of an XY recorder or oscilloscope. It is observed that the polarization-field relationship is not only nonlinear but, if a sufficiently strong field is applied in the positive and then negative direction, hysteresis results.

The subject of dielectric dispersion and adsorption in ferroelectric materials is of considerable interest particularly in connection with ferroelectric transitions. Several references are available which treat this subject in more depth than will be presented here. As applied to shock depolarization, it is understood that dielectric relaxation characteristics are of considerable importance in treating advanced models (7).

For the remainder of this study, the vectorial symbol, $\rightarrow$, will be omitted since in this study the electric field and polarization vectors will always be normal to the electrode surfaces.

2.2 Ferroelectricity

Ferroelectric materials exhibit spontaneous polari-
zation, meaning that they possess an electric dipole moment
in the absence of an electric field. However, the distin-
guishing property that classifies a material as being
ferroelectric is that the direction of spontaneous polari-
zation, called the polar axis, can be reversed by a suf-
ficiently strong electric field.

One of the most prominent characteristics of ferro-
electric materials is the charge-field hysteresis loop.
Figure 1, which is a typical "loop," illustrates hysteresis
along with the well-known nonlinear relationship between
polarization and electric field.

For materials which exhibit hysteresis, equations
of state relationships are difficult to establish because
processes which exhibit hysteresis behavior are irreversible;
thus, parameters cannot be equated by a unique functional
relationship. For ferroelectric materials (see Figure 1),
the intensive parameter (E) is plotted along the abscissa
while the extensive parameter (P) is along the ordinate.
The trace on most virgin ferroelectrics or on most that
have been thermally depoled follows the curve OAB but there-
after as the field varies from E_m to $-E_m$ the curve BCDFGHB
is followed. When E is finally reduced to zero, remanent
polarization of magnitude P_r (or $-P_r$) remains as bound
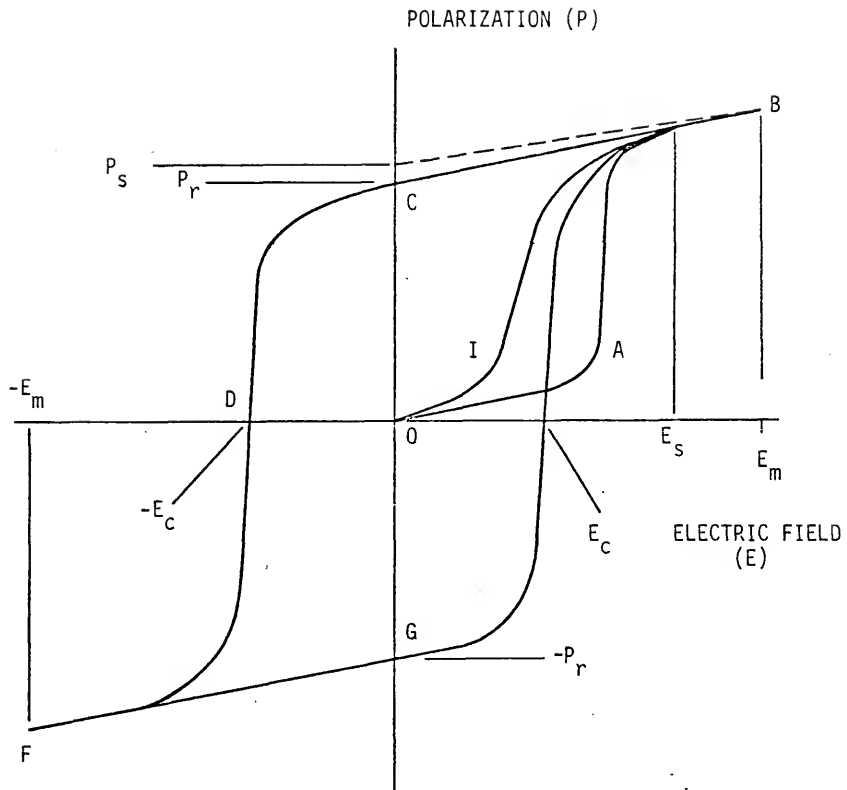
Figure 1. Typical polarization versus electric field hysteresis loop for ferroelectric materials.

charge in the ferroelectric. Curve OIB, called the medium
line, is a tracing similar to that plotted by the initial
trace on a ferroelectric after it has been pressure depoled
(to be discussed later).

Certain features which help to characterize ferro-
electric materials can be defined from the hysteresis loop.
Extrapolation of the linear portion of the tracing above
saturation to the ordinate defines the macroscopic spon-
taneous polarization P_s. The value of polarization where
the loop intersects the ordinate is called the remanent
polarization, P_r. The electric field at which the ferro-
electric becomes saturated is denoted by E_s, while the
electric field required to reduce the polarization to zero
is the coercive field, E_c.

For most ferroelectrics, the polar state exists
only below a certain temperature or in a temperature range.
Above this temperature, which is known as the Curie tem-
perature, T_c, the ferroelectric loses its bound charge and
transforms to the nonpolar paraelectric (PE) phase. Due
to the nonlinear field-polarization behavior, the dielec-
tric constant is usually defined as the slope at the origin
(exceptions to this definition are made in this study;
however, such exceptions are noted). The dielectric con-
stant increases up to the Curie temperature, at which time
it decreases. The Curie temperature is thus defined as
the temperature at which the dielectric constant peaks

(19, p. 382). For many ferroelectrics the Curie tempera-
ture varies depending on whether or not it is being heated
or cooled.

Above T_c, in the nonpolar paraelectric state, the
dielectric constant is described by the Curie-Weiss law,

$$\varepsilon = C/(T - T_o) \qquad (2.2.1)$$

where C is the Curie constant and T_o is the Curie-Weiss
temperature. The Curie temperature is defined as the
temperature at which $1/\varepsilon$ extrapolates to zero when plotted
against temperature. In most ferroelectrics T_o coincides
with T_c; however, there are compositions in which it may
be a few degrees below (10, p. 382).

Most ferroelectric ceramics used in technical
applications belong to a structural class called the oxygen
octahedral group. The unit cell configuration of these
ceramics for the most part is the perovskite subgroup
having the chemical formula ABX_3. Although the perovskite
unit cell is cubic in the nonpolar phase, atomic displace-
ments which cause a slight distortion as it is cooled
through T_c result in less symmetric structures which are
either tetragonal, orthorhombic or rhombohedral.

On a microscopic scale the ferroelectric structure
consists of small ordered regions for which the polariza-
tion vector of each dipole is oriented in approximately

the same direction. These regions are called domains and
a monocrystal or crystallite (if the material is a ceramic)
may consist of many domains as subcells within each grain
which appear under magnification as crystallographic twins.
For two or more adjacent domains the magnitude of spontan-
eous polarization is essentially identical; however, the
polar axis differs.

In a virgin ferroelectric, the macroscopic spon-
taneous polarization is zero due to the randomness of the
domain polarization direction. As an electric field is
applied, the ferroelectric initially behaves as a normal
dielectric (from O to A in Figure 1); however, as the field
increases, domains with a polarization vector closely
aligned with the field grow at the expense of nonoriented
domains (from A to B in Figure 1). Eventually the polari-
zation vector of each domain in the material is aligned as
closely as possible with the polar axis and $\partial E/\partial P$ is constant.
Energetic considerations involving domain formation are
quite complex due to the fact that domain occurrence is
preceded by a nucleation and growth mechanism. Activation
energies required for movement and switching can be of
considerable importance.

Ferroelectric ceramics became functional as a
result of the orientation of domains to favor a selected
direction. This is performed by a process known as poling
which consists of aligning domains by increasing the

electric field to a point above E_s. The ferroelectric is then left in a poled state with a net bound charge equal to P_r.

Domain alignment is associated with the degree of freedom possessed by the B site atom (the center atom) in the perovskite unit cell. In the polar phase, 180° domain reorientation is possible for all structures. Along with 180° switching, domains may reorient by 90° for tetragonal and orthorhombic, 60° to 120° for orthorhombic, or 71° or 109° for rhombohedral (3, p. 48). The orientation of all domains except 180° domains results in an overall distortion of the ferroelectric; consequently, the coercive voltage is less for this type of reorientation. All domains are reoriented during the first few hysteresis loop cycles but thereafter only 180° switching occurs; thus, E_c is a measure of the field required for 180° reorientation. The difference between curve OAK and OHB of Figure 1 is due to the fact that 180° domain switching predominately occurs for curve OIB while 90° and 180° switching occurs for OAB.

Energy conversion in ferroelectrics is attributed to three processes: (1) piezoelectric conversion, consisting of the linear and reversible coupling between elastic and dielectric energy, (2) stress or temperature depolarizing effects due to reorientation of domains, and (3) forced phase transition depolarization in which bound charge is

released by applying sufficient pressure to cause the FE
phase to transform to a PE or AFE phase. The latter two
processes are nonlinear and irreversible. Energetic con-
siderations for all three mechanisms are discussed by
Berlincourt (11). The present study is concerned in part
with the third mechanism, i.e., energy conversion by phase
transitions.

The antiferroelectric transition is one which was
theoretically predicted and explained by Kittel (12, p.
729) prior to its realization. These materials transform
from a nonpolar state to one known as antipolar. Where
it is possible in a FE phase to have other than 180°
domain reorientation, in an AFE phase only 180° domains
are present. While these subcells are polar, the adjacent
subcells are oppositely polarized giving a net polarization
of zero. Domain alignment is such that these materials
possess a center of symmetry; as a consequence, they are
not piezoelectric.

At the AFE-PE transition, the free energy of the
AFE phase for many of these materials is close to that of
an FE phase. Under these circumstances it may be possible
to enforce the FE phase with an electric field. For this
situation a plot of P versus E results in what is known as
a double hysteresis loop (shown in Figure 2). Not all
AFE materials exhibit this behavior; one that does is
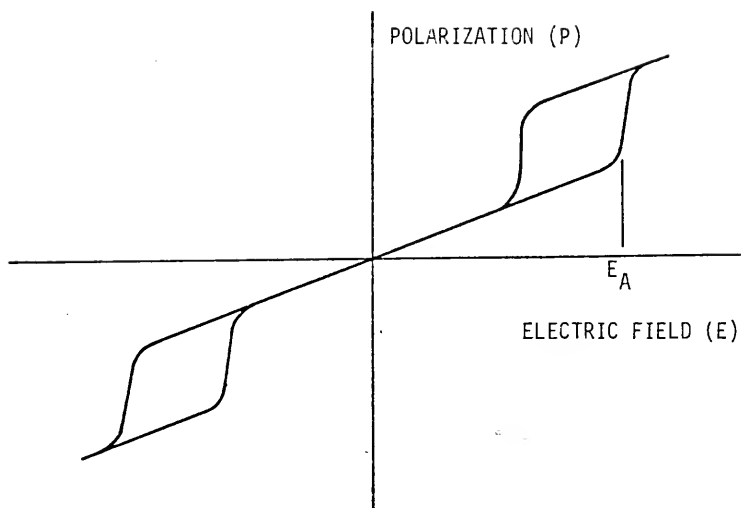termed "soft" (13, p. 1264). The field at which the FE

Figure 2.   Polarization versus electric field for an antiferroelectric
material with field enforced ferroelectricity.
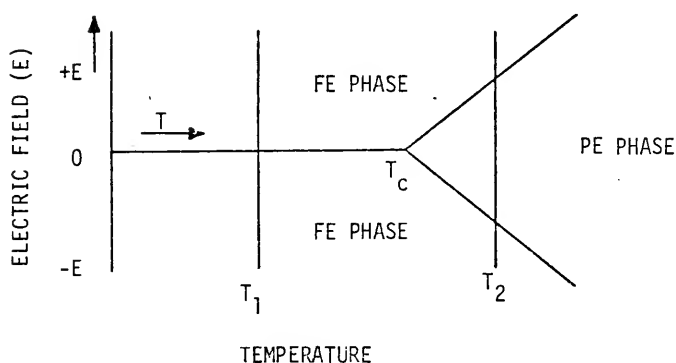

Figure 3.   Electric field versus temperature showing phases encoun-
tered for some ferroelectric materials when looped at T_1
and T_2. At T_2 a double hysteresis loop may result even
though the material is not AFE.

phase is switched (designated as E_A) increases as the free energy between the AFE and FE states widens until the dielectric breakdown strength is exceeded.

Like FE materials, many AFE materials show a high dielectric constant peak near the polar to antipolar transition temperature. It has been suggested that this peak is not associated with the AFE state, but is attributed to the closeness in free energy between the FE and AFE phases at T_c (14, p. 16).

Double hysteresis loops not attributed to anti-ferroelectricity are observable in FE materials that exhibit a polarization change as a result of a bias above T_c. A typical field-temperature phase diagram for such materials is shown in Figure 3. An FE at temperature T_1 would exhibit a normal hysteresis loop, while the same material at T_2 would exhibit the double loop. Thus, the recognition of an antiferroelectric material can be diffi-cult since there appear to be no dielectric test methods that specifically confirm the AFE state. In situations where doubt exists, proof is established by a detailed structural analysis and this information along with dielec-tric measurements can be used to classify it (14, p. 26).

2.3 Ferroelectric Composition PZT 95/5

In 1953, Sawaguchi (2, p. 624) presented a PZT temperature-composition phase diagram similar to that shown

in Figure 4. The most studied compositions lie near the 50-50 morphotropic phase boundary because of the enhancement of the piezoelectric properties as this boundary is approached. In Figure 4, the dotted line designating the FEI-FEII boundary in the FEA phase was first noted by Barnett (15). At this boundary there is a dielectric anomaly and a change in thermal expansion; however, x-ray analysis shows the structure on either side to be rhombohedral (15).

PZT 95/5 was developed primarily for shock depolarization purposes. As seen in Figure 4, the composition is in close proximity to the AFE-FE polymorphic phase boundary. With pressure the phase boundary is caused to displace to the right; i.e., the AFE phase is preferred over the FE phase.

The peculiar polarization behavior of lead zirconate was first observed by Roberts (16) in 1950. However, it has been noted (17, p. 123) that Sawaguchi was the first to describe its behavior as antiferroelectric. In Sawaguchi's 1953 paper (2), the properties of lead zirconate with small quantities of lead titanate as determined by structural analysis, dielectric measurements, heat capacity measurements, and dilatometry were presented. In the tetragonal antiferroelectric phase (AFE_B), it was shown that it was possible to enforce ferroelectricity which resulted in a double hysteresis loop. This was not
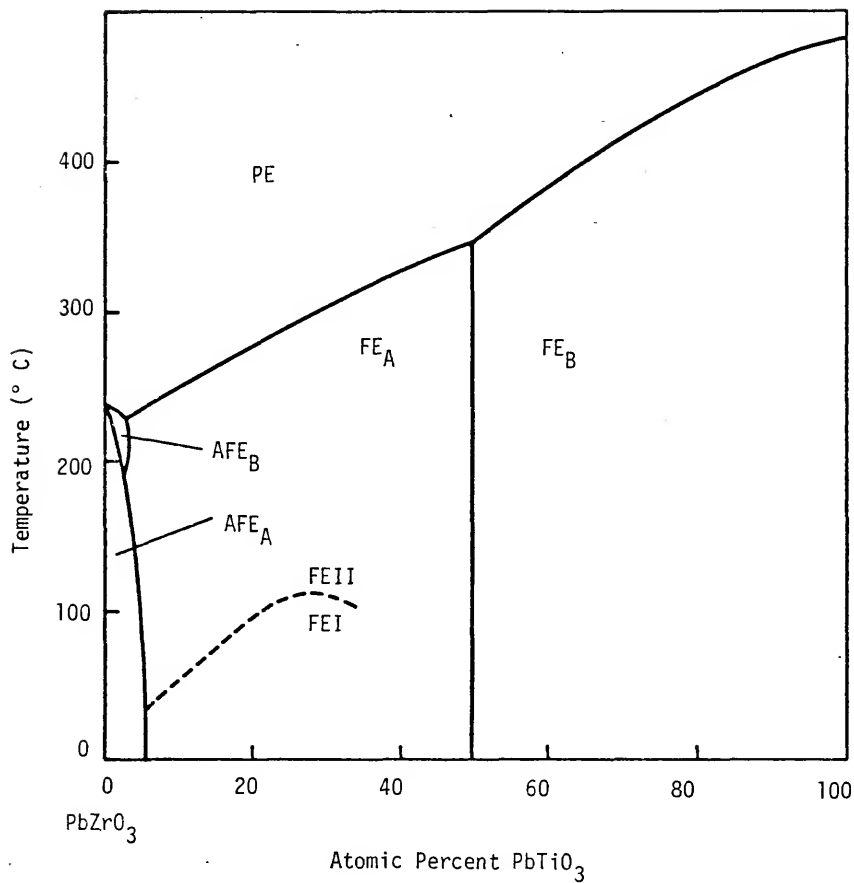
Figure 4. Temperature versus composition phase diagram for lead zirconate-lead titanate (no niobium). This plot is similar to that developed by Sawaguchi (2, p. 624) except for the added FEI-FEII boundary noted by Barnett (15).

possible for the AFE_A phase. Additional phase diagram studies made by Berlincourt and Krueger (18, p. 3) showed that the AFE_B phase was observed only on tests made with increasing temperature.

These phase diagrams as well as similar diagrams on other ferroelectric materials show two phases separated by a single line rather than a two-phase region as required by the Gibbs phase rule. Jaffe et al. (15, p. 136) have confirmed that two phases actually are in equilibrium between the FE_A and FE_B phases of PZT, but because of the narrowness of the boundary, detection methods usually result in a single peak. This is partially due to metastable phase which transform rapidly after initiated. To be more descriptive, some authors refer to these dia-grams as "transitive temperature-composition" diagrams.

For the present project the specific PZT composi-tion is $Pb_{.995}(Nb_{.01}(Zr_{.95}Ti_{.05})_{.99})O_3$. This is commonly referred to as PZT 95/5 with 1% niobium or just PZT 95/5. Niobium in small percentages is added to many PZT ferro-electric ceramics to improve electrical resistance at high temperature. For PZT 95/5 it was found that by vary-ing Nb_2O_5 between 0.5 and 1.5%, the depoling pressure varied directly. However, because of fluctuations in manufacturing methods, chemical impurities, pore size, grain size, etc., the precise dependence of depoling pres-sure on Nb_2O_5 was difficult to establish. In order to

obtain a composition with a desired depoling pressure, it was necessary to adjust the niobium content on a small portion of a large batch until the correct depoling pressure was attained; the remainder of the batch was then corrected and processed. For this reason the exact amount of niobium present in the ceramics used in this study was not known.

The effects of niobium on the PZT system near the pure lead zirconate composition has been examined by Dungan et al. (19), Berlincourt and Krueger (18), and Torccaz et al. (20). The room temperature ternary diagram of compositions between 100% $PbZrO_3$, 10% $PbTiO_3$, and 10% $PbNb_2O_6$ determined by Dungan et al. (19, p. 384) is shown in Figure 5. As niobium increases, the FE phase of a composition containing 5% $PbTiO_3$ becomes further from the AFE phase which is what would be expected from pressure depolarization results reported by Berlincourt and Krueger (18).

A lead zirconate-lead titanate compositional-temperature phase diagram with 2.5% Nb by Dungan et al. (19, p. 385) and diagrams by Berlincourt and Krueger which contain 1% Nb (18, p. 18) and 2% Nb (18, p. 22) do not show the AFE_B phase. This indicates that this phase is possibly nonexistent for PZT materials containing niobium. However, a low temperature AFE phase appears in the compositional-temperature phase diagram developed by Torccaz et al. (20). The significance of this is not known; it is believed that the phase occurs only upon cooling.
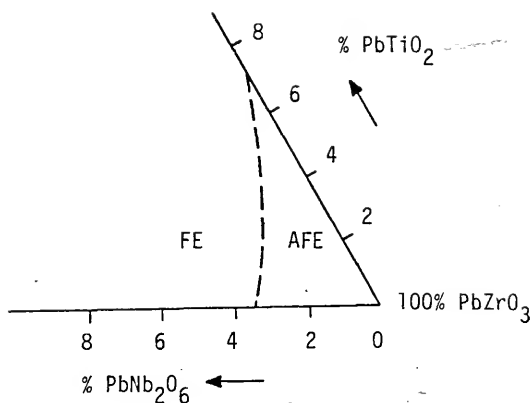
Figure 5. Ternary compositional phase diagram at room temperature for $PbZrO_3$, $PbTiO_2$, and $PbNb_2O_6$ near the 100% $PbZrO_3$ composition (19, p. 384).
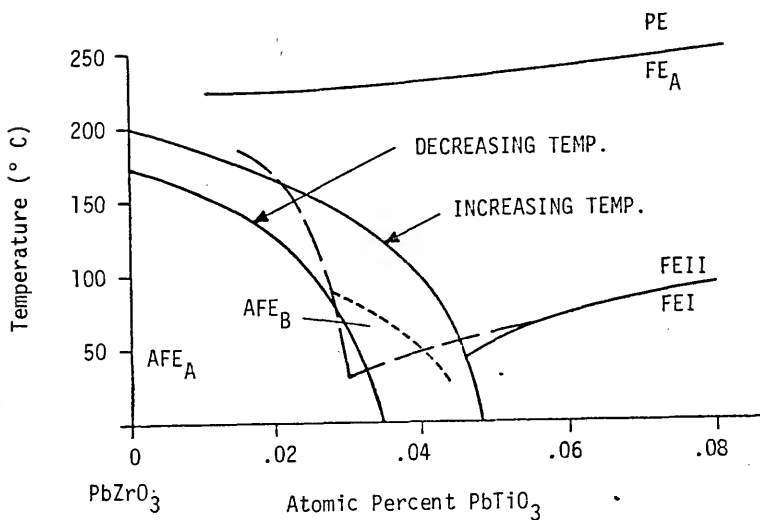

Figure 6. Temperature compositional phase diagram for lead zirconate-lead titanate with 1% Nb_2O_5 as developed by Berlincourt and Krueger (18, p. 18) as shown as solid lines, and by Torccaz et al. (20, p. 597) as shown by dashed lines.

The 1% Nb phase diagram developed by Berlincourt
and Krueger (18, p. 26) along with the Torccaz et al. 1%
Nb diagram (20, p. 597) is shown in Figure 6.

2.4 Ferroelectrics at High Pressure

Pressure effects on the properties of ferroelec-
trics have been examined using both static (hydrostatic
and quasihydrostatic) and dynamic (stress waves and shock
waves) techniques. Because of the pressure-sensitive
characteristics of ferroelectrics, the use of static
techniques has been a popular area of investigation.
Earlier static experimental studies have been confined
to relatively low pressures (<1 GPa). However, within the
last 15 years higher pressure results have been reported.

Pressure investigations on ferroelectrics have
been most extensively performed on barium titanate. Samara
(21) has investigated the effect of both pressure and
temperature on monocrystals as well as polycrystalline
$BaTiO_3$ up to 2.5 GPa. He found that for both types of
samples, the Curie temperature decreased linearly with
pressure (21, p. 172). However, an interesting difference
between the samples was observed; the permittivity of the
monocrystal (taken along with the "c" axis) increased near
the FE-PE transition by 60 to 70% as pressure increased up
to 1.5 GPa while that of the ceramic decreased by over 50%

in the same pressure range. It appears that this is related to the pressure dependence of the permittivity along the "a" axis (ε_a). For these measurements ε_c, not ε_a, was determined on the monocrystal and since the length of the "c" axis decreases with pressure faster than the "a" axis, it is reasoned that domains in the "c" direction switch to the "a" direction, causing ε_c to increase. For the macroscopically isotropic ceramic, an average value of ε is measured. Ceramic porosity was not considered as a contributing factor because the denser ceramics showed a larger decrease in ε (10, p. 382).

Samara found that the permittivity of $BaTiO_3$ (22, p. 281), $SrTiO_3$ (23, p. 378), and $PbTiO_3$ (22, p. 282) obeyed a Curie-Weiss type relationship in the high pressure nonpolar (PE) phase, i.e.,

$$\varepsilon = C^*/(p - p_0) \qquad\qquad (2.4.1)$$

where C^* and p_0 are constants with p_0 equal to the pressure at which $1/\varepsilon$ extrapolates to zero when plotted against pressure.

It was also observed that for $BaTiO_3$ (10, p. 380) the remanent polarization as well as the coercive field gradually decreased up to the Curie temperature at which time the loop took on the form of a double hysteresis loop.

Examinations above 2.5 GPa have been performed on SrTiO$_3$ (up to 5 GPa) by Samara and Giardini (24) using a tetrahedral anvil device. In these experiments the pressurization medium was AgCl which is considered to be quasi-hydrostatic at these pressures.

Polandov et al. (25) have examined polycrystalline PZT 53/47 with 1% Nb$_2$O$_5$ at quasihydrostatic pressures up to 8 GPa. The results showed a gradual decrease in ε from 2 to 2.3 GPa; ε then increased and peaked at a value of 3.6 to 4 GPa and then gradually decreased. The decrease in ε at 2 to 2.3 GPa was attributed to the breakup of the crystallites (due to void collapse) at which time the domain configuration was rapidly changing causing an anomaly in ε. When the material took on more stable domain configuration, the dielectric constant increased. The reason ε peaked at 3.6 to 4 GPa was not explained.

A limited amount of static high pressure information is available on PZT 95/5. Berlincourt and Krueger (18, p. 110), developed a pressure-temperature phase diagram for PZT 95/5 (see Figure 7) that showed pressure favoring the AFE phase. At ambient temperature the FE-AFE transition occurred at 0.14 GPa. Hydrostatic studies have been performed by Gonnard et al. (26) on a PZT 95/5 type ceramic (PbZr$_{.95}$Ti$_{.05}$O$_3$+.8 WO$_3$) in which a transition pressure of 0.18 GPa was reported.
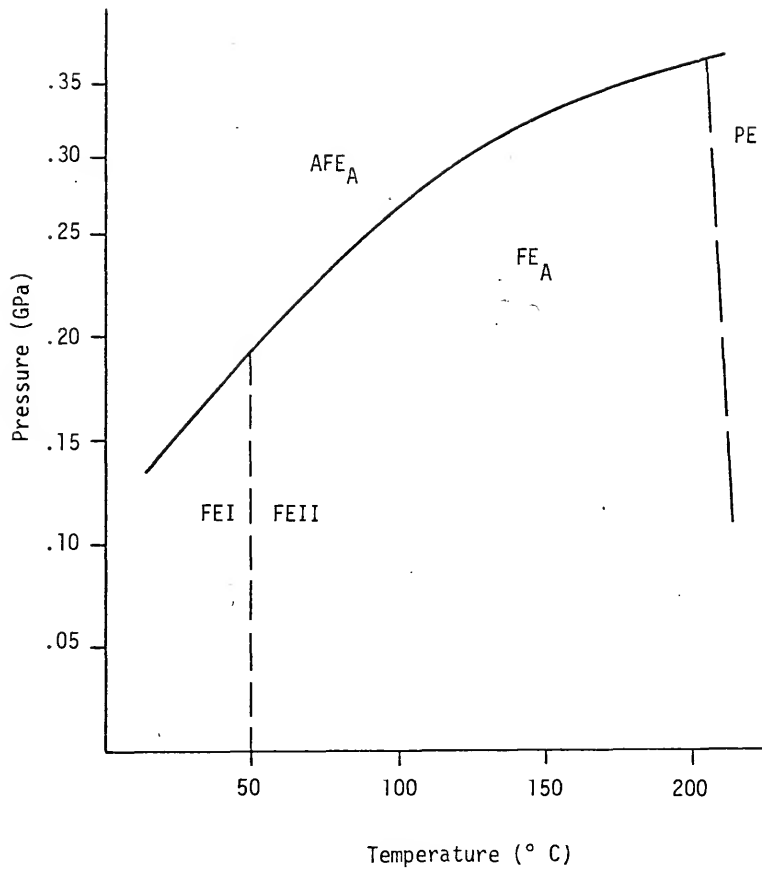
Figure 7. Pressure versus temperature phase diagram for $Pb_{.995}Nb_{.01}(Zr_{.95}Ti_{.05})_{.99}O_3$ as developed by Berlincourt and Krueger (18, p. 110).

Numerous theoretical studies have been made on the dynamic depolarization mechanisms in ferroelectrics (1, 4, 5, 6, and 27). Also, experimental investigations on the effect of shock waves in ferroelectric materials such as $BaTiO_3$, PZT 52/48, PZT 65/36 and PZT 95/5 have been reported (27, 28, 29, 30, 31, and 32).

Of importance in the experimental studies has been the appearance of a two-wave shock structure; i.e., the wave does not consist of a single step but propagates as two components of different stress amplitudes. This was first noted by Nielson on barium titanate and PZT 52/48 ceramics (28, p. 1402). Shortly thereafter, Reynolds and Seay (28, 29) confirmed these results. Similar observations were seen on PZT 95/5 by Halpin (27), Doran (30, 31), and Linde (32). (In one instance a three-wave structure was reported by Doran.)

Multiple-wave shock structures are attributed to either phase changes or material rigidity. Regarding the former mechanism, numerous examples of shock induced phase transformations were described by Lysne et al. (33) in a review of this subject. For $BaTiO_2$ and PZT 52/48, Reynolds and Seay (29) attributed the observed two-wave structure to rigidity effects due to the fact that on samples tested above the Curie temperature, the two-wave structure persisted and when the amplitude of the initial wave was plotted versus temperature, it appeared to be continuous

through the Curie temperature. They attribute the loss of
remanent polarization to a reduction in dipole moment by
axial compression rather than by domain reorientation.
As a result of their studies, a Hugoniot was constructed
which showed an elastic cusp of 2.3 GPa for BaTiO$_3$ with
a steady shock threshold of 48 GPa and for PZT 52/48 an
elastic cusp of 1.9 GPa with a steady shock threshold of
21 GPa.

For shock depolarization studies performed on PZT
95/5, Doran (31, p. 46) found the amplitude of the first
wave varied between 2.1 and 4.8 GPa depending on the initial
density. Halpin (27) examined PZT 95/5 up to 3.3 GPa and
found the first wave amplitude to be 0.5 GPa; thus, he
suggested that it was associated with the FE-AFE transi-
tion. Except for one sample, all of Halpin's ceramics
were hot pressed.

None of the above references mentioned collapse of
voids as a possible cause of the multiple-wave shock struc-
ture. However, in a recent analytical study, Nunziato and
Walsh (34) showed the existence of two distinct accelera-
tion waves in a granular solid with porosity. Using a
model for a granular material proposed by Goodman and
Cowin (35), they showed that an acceleration wave moving
into such a material would decompose into two waves, one
associated with the compressibility of the granules and
the other associated with the void collapse. Although

that work has not yet been extended to shock and higher-order waves, it is expected that a similar two-wave structure will exist for shock propagation.

2.5   High Pressure Static Test Apparatus

Prior to the mid-1950's, ultrahigh pressure testing for the most part had been confined to the flat anvil apparatus developed by P. W. Bridgman. This was a uniaxial piston-anvil device in which the geometry of the tungsten carbide anvils and steel binding rings was such as to provide optimum lateral support to the anvil surface in contact with the specimen. With the complete press under 3 GPa isostatic pressure, it was possible to subject a specimen to over 45 GPa (36, p. 271). Much of the success of this unit was attributed to the pipestone (catlinite) compressible gasket used to contain the test specimen.

In 1958, Hall (36) described a three-dimensional press which incorporated the pressure-transmitting features of Bridgman's two-dimensional flat anvil apparatus. This device, called the tetrahedral anvil apparatus, applied uniform pressure to the faces of a regular tetrahedron fabricated from the mineral pyrophyllite.*

---

*Hydrous aluminum silicate ($3Al_2O_3$-$4SiO_2$-H_2O). Pyrophyllite is also known as wonderstone or Tennessee Grade A Lava® (a product of 3M Corporation, Chattanooga, Tenn.).

Hall selected pyrophyllite over pipestone because it was more readily available and more machinable. However, because pipestone contains iron oxide (known for its high coefficient of friction), it is preferred for ultrahigh pressure testing.

Hall's original design consisted of four hydraulic cylinders or rams positioned so that their anvil faces were parallel with the faces of the tetrahedron while their centerline intersected at the center of the tetrahedron. The rams were held in place with tie-rods. In addition to this tie-rod unit, some variations in the tetrahedral press have been introduced. A popular unit capable of 9.0 GPa, called the NBS unit, was devised by Lloyd, Hutton, and Johnson (37). For this unit, the driving force was applied to a single (upper) anvil rather than all four anvils. The resultant forces were transmitted to the three remaining (bottom) anvils.

Another unit quite similar to the tie-rod unit replaced the ram-tie-rod structure with four steel forgings (called platens) which were connected by hinges. A large diameter cavity in the platen contained a pressure-transmitting piston. This type of unit was called the hinged tetrahedral anvil apparatus and is the type of device used in the present study.

The sample for these pressures was located at the center of the pyrophyllite tetrahedron. Pressure applied

to the sample was dependent upon the ability of the pyro-
phyllite to act as a pressure-transmitting medium without
excessively extruding between the anvils. Along with
transmitting pressure, the pyrophyllite imparted thermal
and electrical insulation and provided material for the
necessary gasket. The edges of the tetrahedron were pur-
posely longer than the legs of the triangular face of the
anvil so that the gasket could be formed by extrusion
of the pyrophyllite between adjacent anvils during the
initial pressurization stages. The necessity of the
gasket is appreciated when one considers that at high
pressures it is possible to subject the tetrahedron to
pressure variations from 10 GPa to 100 kPa in a distance of
1 to 2 cm.

For pyrophyllite, Hall (36, p. 272) suggested an
edge length 125% longer than the anvil triangle legs.
This ratio has been confirmed by others (38, p. 1321).
To limit the flow of pyrophyllite at the anvil faces,
jeweler's rouge (Fe_2O_3), suspended in an organic solvent,
has sometimes been painted on the faces of the tetrahedron.
With its high friction coefficient of 0.71 (39, p. 4),
the lateral movement of the pyrophyllite relative to an
anvil face was reduced.

The test specimen can be placed within the pyro-
phyllite tetrahedron in various ways. The three most
common configurations are shown in Figures 8, 9, and 10.

PYROPHYLLITE

METAL ELECTRICAL CONTACT TABS
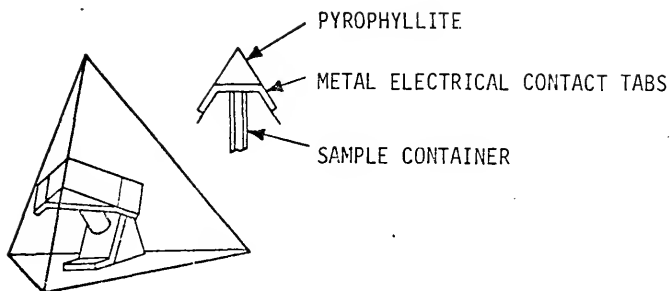
SAMPLE CONTAINER

Figure 8. Edge-to-edge test sample configuration used by
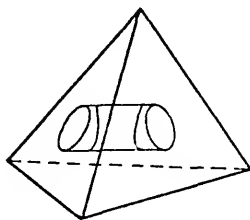Hall (36, p. 272) in the tetrahedral anvil device.

Figure 9. Face-to-face test sample configuration used by Lees (40,
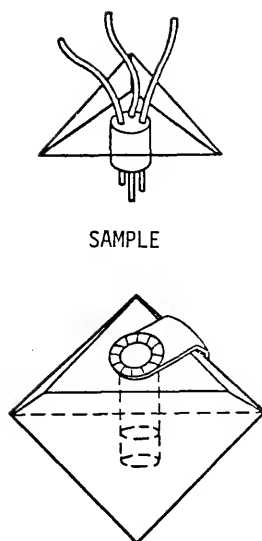p. 967) in the tetrahedral anvil device.

SAMPLE

Figure 10. Face-to-vertex test sample configuration used by Decker
et al. (41, p. 332) in tetrahedral anvil device.

Figure 8, called the edge-to-edge configuration, resembles Hall's original design (36, p. 272). Figure 9, called the face-to-face configuration, has been used by Lees (40, p. 967). Figure 10, called the face-to-vertex configuration, was used by Decker et al. (41, p. 332) and can be used to make simultaneous electrical measurements on samples contained within a true hydrostatic pressure environment. This is the sample configuration selected for this study; details of its construction are presented later.

CHAPTER 3
EXPERIMENTAL PROGRAM

3.1 Tetrahedral Anvil Apparatus

The tetrahedral anvil apparatus along with the control console and an instrumentation module used for this study are shown in Figure 11. This unit* is known as the 600/2400 ton model which designates a device in which a maximum of 600 tons of force can be transmitted by each of the four pistons.

Prior to the initiation of this project, the press had been in storage. The elapsed storage time was unknown but it was suspected that corrosion damage to the pistons or cylinder walls had occurred since the pistons were not removed from the platens prior to storage and since it was known that the manufacturer recommended water (with a rust preventative) as the pressurization medium. Upon removal of all pistons, corrosion damage (as shallow pits) was observed on all cylinder walls with one cylinder showing an extensive amount of damage in the form of two

---

*Fabricated by Barogenics Corporation, New York, N. Y.

Figure 11. The 600/2400 ton tetrahedral anvil apparatus along with
the control panel and the low voltage looping module
used for these studies.

deep corrosion pits. These, as well as the shallow pits, were filled with Epocast 40 ® * tooling epoxy and blended with the cylinder wall using 600 grit emergy paper. After reassembling, the hydraulic system was recharged with Harmony 44 ® ** SAE 5 oil.

A description of the press, along with modification performed on the press and the operation instructions, is given in Appendix A.

3.2 Test Cell

Details concerning the fabrication and assembly of the test cell and tetrahedron, along with information regarding the dielectric fluid, ferroelectric samples and manganin,*** are all given in Appendices B through G. The face-to-vertex cell configuration shown in Figure 10 was used for this study. The manganin cell and FE test sample were positioned in a thin-wall stainless steel cylinder which was filled with a 1 to 1 mixture by volume of pentane and isopentane and capped at each end with

---

*Furane Plastics, Fairfield, N. J.

**Gulf Oil Co., Houston, Tex.

***Manganin is an alloy whose resistance varies with pressure but not temperature in a range about room temperature. The composition will vary depending on manufacturer. Typical compositions are 87% Cu-13% Mn and 83% Cu-13% Mn-4% Ni where the composition is in weight percent.

polyethylene plugs. A cross-sectional view of the final
test assembly is shown in Figure 12.

3.3   Instrumentation and Measurement Technique

The resistance of the manganin cell was determined
by applying a 10-ma current to the cell and measuring the
voltage drop with a Model H.P. 3460A* digital voltmeter.
This has an accuracy of $\pm$ 0.002% with six place resolution.
An H.P. Model 256* printer was adapted to the voltmeter.
This was capable of printing the voltmeter output to five
places on demand or at a continuous rate. The current
supply (HP351)* used was accurate to $\pm$ 0.05%; however,
prior to and following each test series the actual current
was determined by substituting a standard 100-ohm resistor
accurate to $\pm$ 0.005% in place of the manganin cell.

Charge-field hysteresis loops were performed using
a low voltage looper (the schematic is shown in Figure 13).
Peak voltage up to 3000 volts could be selected while the
looping period could be varied from 28 to approximately
500 seconds. It was possible to subject a sample to an
entire loop or merely to pole it. The voltage output with
time is linear; thus, a triangular-shaped wave resulted.
Two integrating capacitors could be switched in and out of

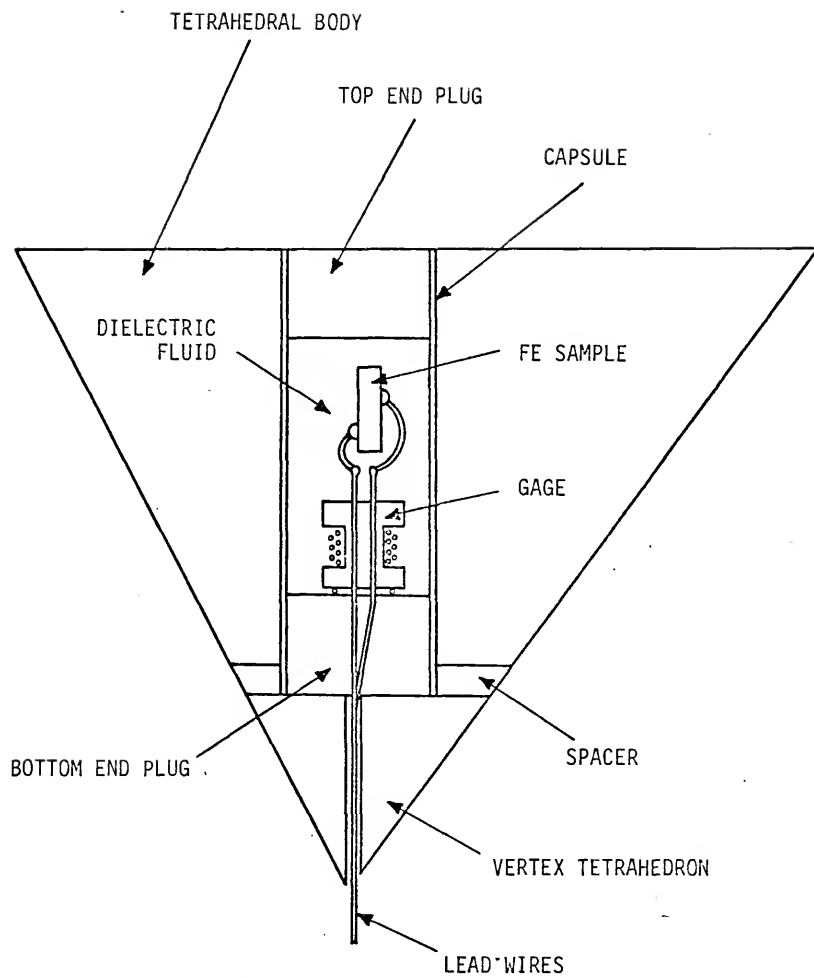*Hewlett-Packard, San Diego, Calif.

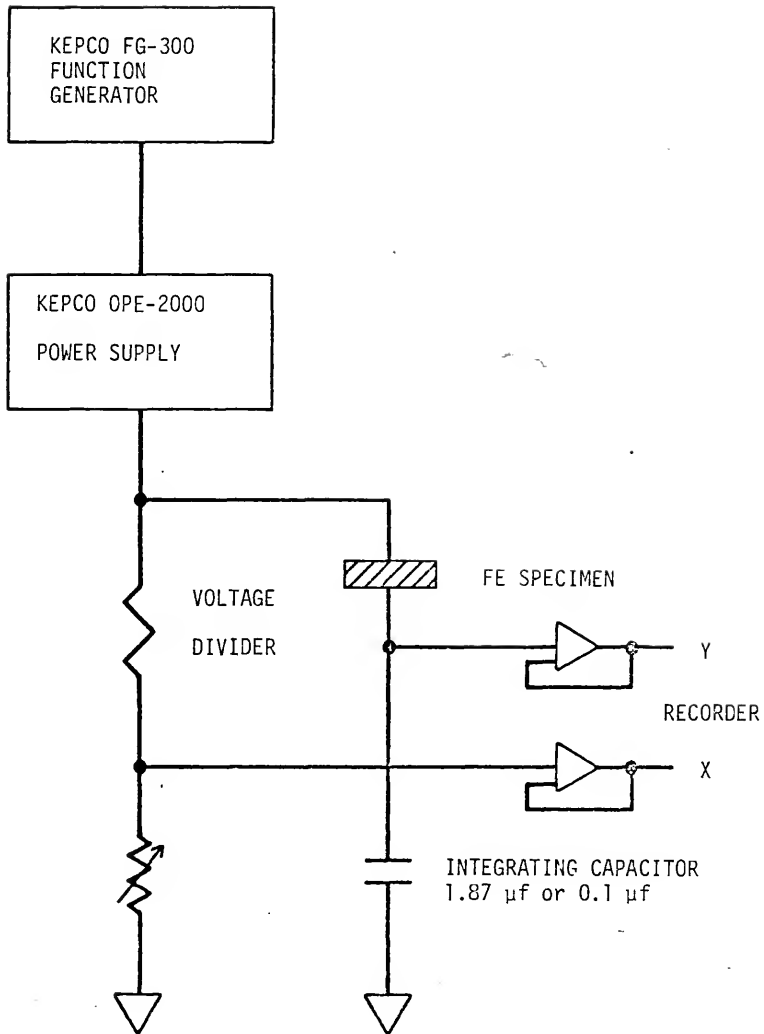Figure 12. Cross-section of test capsule as positioned in pyro-phyllite tetrahedron.

Figure 13. Schematic of hysteresis looper used for poling and loop-
ing ferroelectric specimens.

the circuit. A 1.87 μf capacitor was used for looping
while a 0.1 μf was used for poling. The trace was recorded
on an H.P. 7046A* XY recorder.

The poling curve was   used to measure polari-
zation at high fields. When the ferroelectric was tested
below the FE-AFE transition the poling curve was quite
lossy; thus, the curve was retraced four to five times
until the final stabilized curve was obtained. Since the
curve is nonlinear, a dielectric constant was arbitrarily
determined by measuring the slope from the origin to the
point on the curve intersected at an electric potential
of 1000 V.

Dynamic dielectric measurements were made using
an HP4270* automatic capacitance bridge. Both capaci-
tance and dissipation factor were determined to four
significant places. Frequencies of 1 kHz, 10 kHz,
1000 kHz and 1 MHz were available. The accuracy of this
unit is $\pm$ 0.1% for capacitance and $\pm$ 0.01% for dissipa-
tion factor.

3.4   Test Procedure

Three areas of experimental interest were examined.
The first concerned the behavior of PZT 95/5 at the FE-AFE

---

*Hewlett-Packard Corp., San Diego, Calif.

phase change, the second concerned its behavior immediately
after the phase change in the nonpolar phase, and the
third concerned high pressure dielectric anomalies.

Measurements consisted of initially determining
the dynamic capacitance and dissipation factor at the
four frequencies available, looping two or more times,
poling five or more times, and then repeating the dynamic
measurements. This measuring schedule usually took 7 to
10 min and continued pressurization of the press was
halted during these measurements. There were exceptions
to this measuring procedure; in some instances only the
capacitance at 1 kHz was measured while the pressure to
the sample was slowly increasing or decreasing. Above
the FE-AFE transition, looping was usually omitted and
only the poling plot was determined.

For measurements relating to the FE-AFE phase
transition behavior, the usual pressure change increment
between measurements was 50 psi on the Heise gage except
near the phase change where the increment size was reduced.
At pressures above the FE-AFE phase change the Heise gage
pressure increment was usually 250 psi. Where possible,
this increment was reduced near the high pressure anomaly.

A formal error analysis of the data was not per-
formed. The reason is that the sample-to-sample scatter
was considerably larger than any other source of error.

Rather than present all data, only typical data which are most representative are shown.

3.5   Data Analysis

.From hysteresis loops the coercive field and remanent polarization were determined. The coercive field of the loop was calculated by measuring the width of the loop at zero polarization and dividing by two times the sample thickness. Remanent polarization was found by determining the height of the loop (in μ coul) at zero and dividing by two times the surface area of the sample. Due to the large integrating capacitor used (1.87 μ coul), it was not necessary to correct for lead wire capacitance.

A typical poling curve is shown in Figure 14. Only the static dielectric constant was determined from the trace; this was specified by the author in an arbitrary fashion. Polarization was taken as the point on the curve where a perpendicular line at 1000 V intersects the lower portion of the tracing. The dielectric constant was then found by determining $\Delta P / \Delta E$. This value was divided by ε_o to determine the relative dielectric constant. A lead wire correction was made by subtracting a predetermined value of 32 from the calculated dielectric constant.
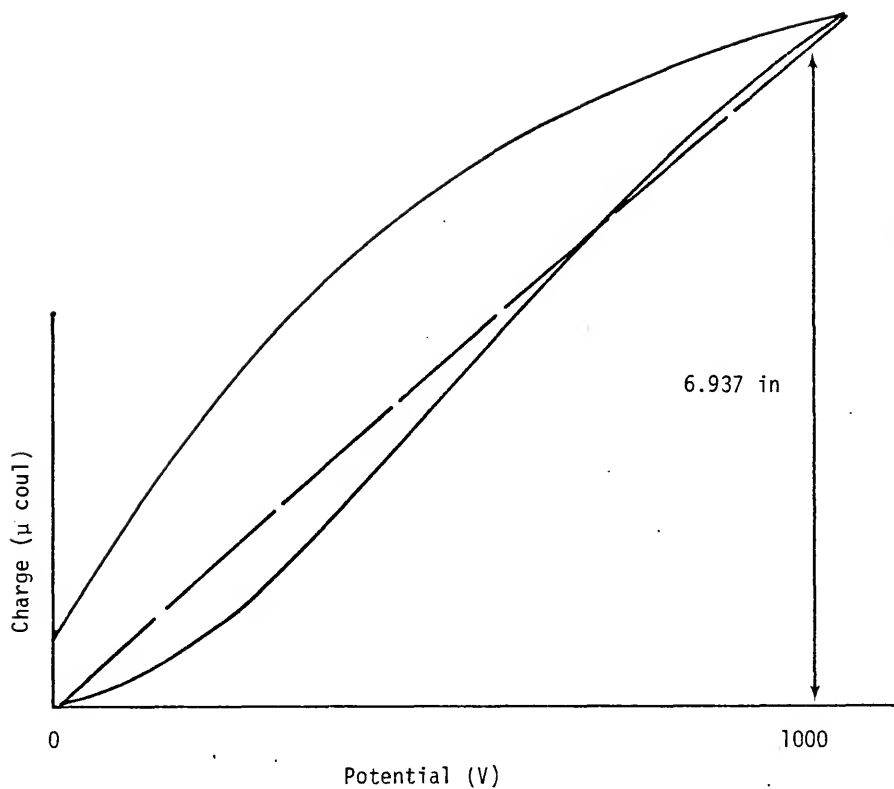
Figure 14.   Charge versus potential poling trace for PZT 95/5 ferroelectric ceramic. Dielectric constant measurements were based on the slope from the origin to the curve at 1000 V.

This is the dielectric constant obtained when the lead wires are run without a ferroelectric.

Small signal dielectric constant measurements were made which determined the sample capacitance and dissipation factor. The following lead wire corrections were made to the capacitance value by subtraction: 1 kHz = 1.29 µf, 10 kHz = 1.277 µf, 100 kHz = 1.268 µf, and 1 MHz = 1.260 µf. Only a subtraction of 0.0014 from the 1 MHz dissipation factor was made; the rest were zero. Dielectric constant was determined by multiplying the capacitance by the thickness and dividing by the area. Relative dielectric constant was calculated by dividing by ε_o. This gave a value of K or K'. To find K" it was not necessary to multiply K' by the dissipation factor as was shown in section 2.1.

During the testing the sample was obviously elastically deformed (and by pore collapse plastically deformed). The dimensional changes resulting from this deformation were not taken into consideration.

CHAPTER 4

RESULTS

4.1   Overall Results

Permittivity data for application in depolariza-
tion models may take many forms. In the simplified models
of Nielson (1) and Anderson (4), first-order approximations
of permittivity in the shocked and unshocked regions as
a shock traverses the sample were sufficient. Other
models incorporated provisions for pressure dependent per-
mittivity even though high pressure data on most ferro-
electric materials had not yet been determined (5, 6, 27).
The present state of the art has advanced to the point
where dielectric relaxation data at each pressure and tem-
perature are desired (7). This would require a detailed
frequency scan of the sample to establish ε_i, ε_s, and the
permittivity at frequencies in between ε_i and ε_s. The final
section of this chapter will discuss this subject. Much
of the information in the other sections of this chapter
may appear to be of academic interest; however, due to
the complicated nature of pressure depolarization phe-
nomena, especially in the region behind the shock front

49

where the pressure varies and the electric field may vary, the results should provide a better understanding of the dynamic depolarization process.

Figure 15 is typical of the pressure dependent dielectric behavior (shown as small signal K at 1 kHz versus pressure) of PZT 95/5. In this plot the dielectric constant gradually increases and peaks at the FE-AFE transition; it then abruptly drops and gradually levels off at higher pressures. For the sample shown in Figure 14, hysteresis looping was performed at each measurement interval. For this type of test the average FE-AFE phase transition on six samples occurred at 0.32 ± 0.04 GPa.

It was possible to loop PZT 95/5 at pressures up to the FE-AFE transition. When looping was attempted in the AFE phase, the resulting trace resembled that taken on a "lossy" capacitor. The "lossiness" was greater near the transition than at higher pressures. At pressures immediately following the transition, attempts were made to induce the FE phase by increasing the voltage, but dielectric breakdown occurred.

The initial loop on a typical sample is shown in Figure 16A. Since it had been thermally depoled by heating above the Curie temperature during vacuum drying, 90° as well as 180° domain reorientation (as discussed in Section 2.2) is evident. Figure 16B shows the initial loop on a sample at zero pressure after the sample had been pressure
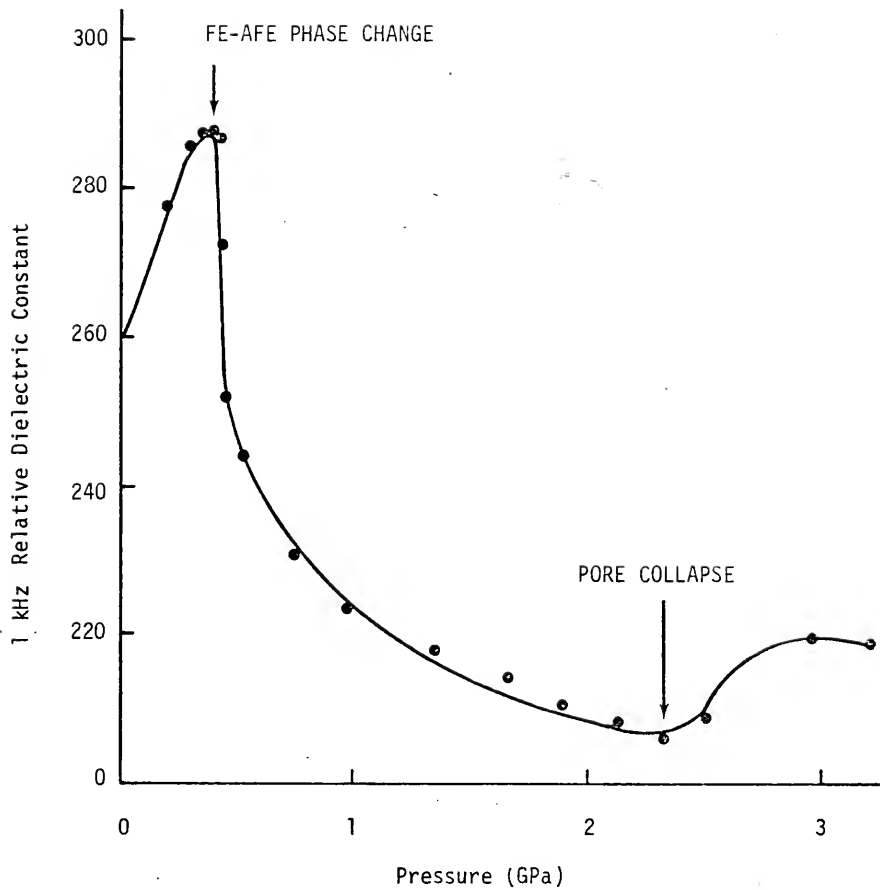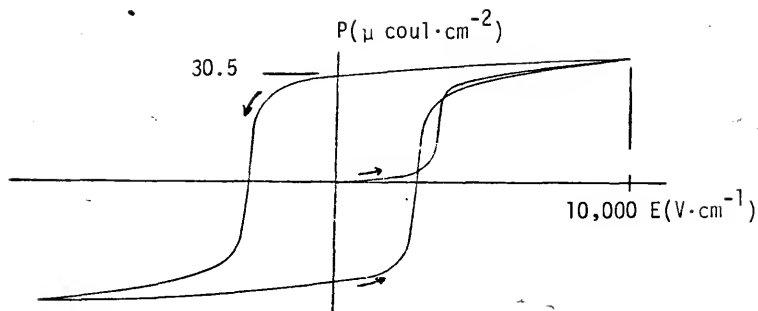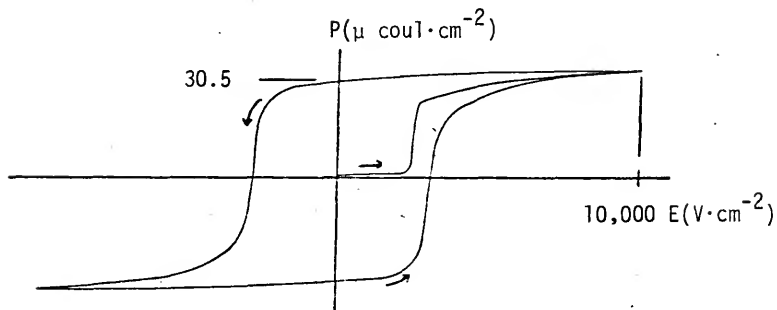
Figure 15. 1 kHz small signal relative dielectric constant versus pressure for PZT 95/5 ferroelectric ceramic.

P(μ coul·cm^{-2})

30.5

10,000 E(V·cm^{-1})

a

P(μ coul·cm^{-2})

30.5

10,000 E(V·cm^{-2})

b

Figure 16. Polarization versus electric field hysteresis loop on
a thermally depoled PZT 95/5 ferroelectric ceramic.
a. Both 90° and 180° domain reorientation are evident
from the initial trace.
b. Predominantly 180° domain reorientation is evident
from the initial trace.

depoled. In this case only 180° domain reorientation is evident. The 180° domain structure is characteristic of the AFE state so it is possible that the AFE domain structure was retained during depressurization.

The variation of remanent polarization and coercive voltage with pressure up to the transition is shown in Figure 17. It is believed that the remanent polarization discontinuity at the transition pressure is sufficient to verify that the transition is first order.

As mentioned previously, three or more loops were performed at each pressure to assure a stable and repeatable loop. At or near the phase transition, it was possible to induce the nonpolar phase by continued looping. The polarization decreased each time the specimen was looped until the nonpolar phase was attained. A series of loops representing this condition is shown in Figure 18.

A graph showing the variation of dielectric constant as measured from the poling trace is shown in Figure 19. At the transition pressure, K increases substantially and the poling trace becomes quite "lossy" as shown in Figure 20. The initial slope of the poling curve is less than that at higher voltages; as a consequence, the small signal relative dielectric constant is lower than the relative dielectric constant shown in Figure 19. After the transition, the difference between these values decreases because the poling traces become less "lossy" at higher pressures.
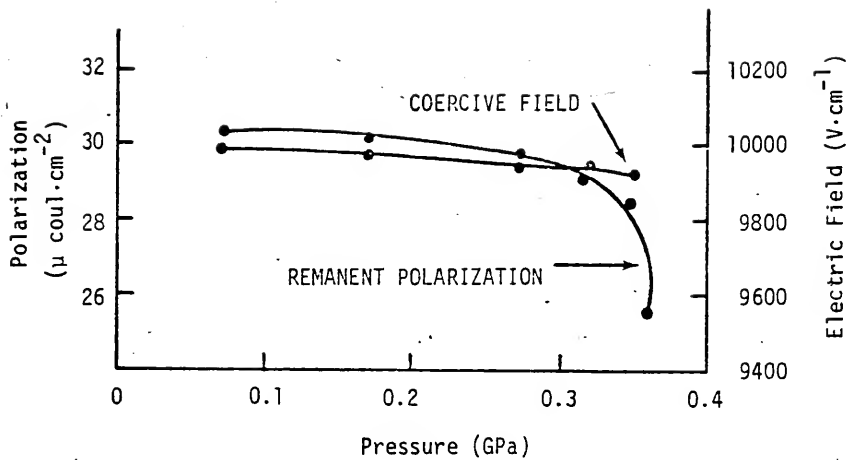
Figure 17. Remanent polarization and coercive voltage versus pressure as measured from hysteresis loops on a PZT 95/5 ferroelectric ceramic.
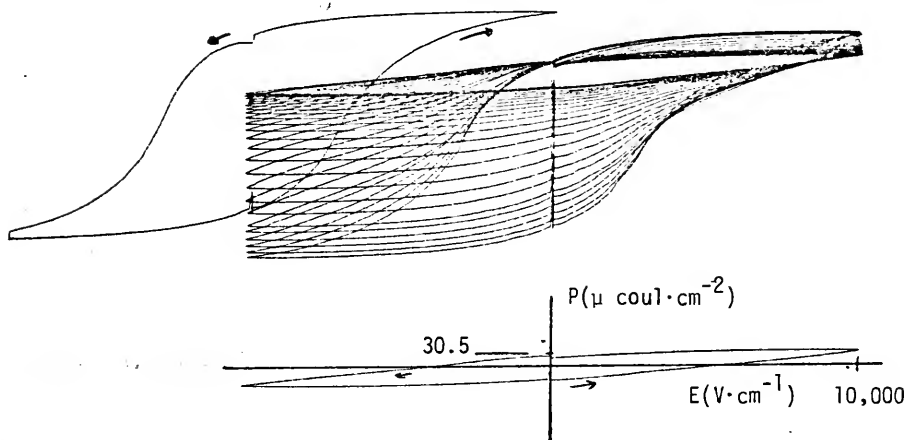

Figure 18. Polarization versus voltage hysteresis loops illustrating how looping can induce the AFE phase at or near the transition of a PZT 95/5 ferroelectric ceramic.
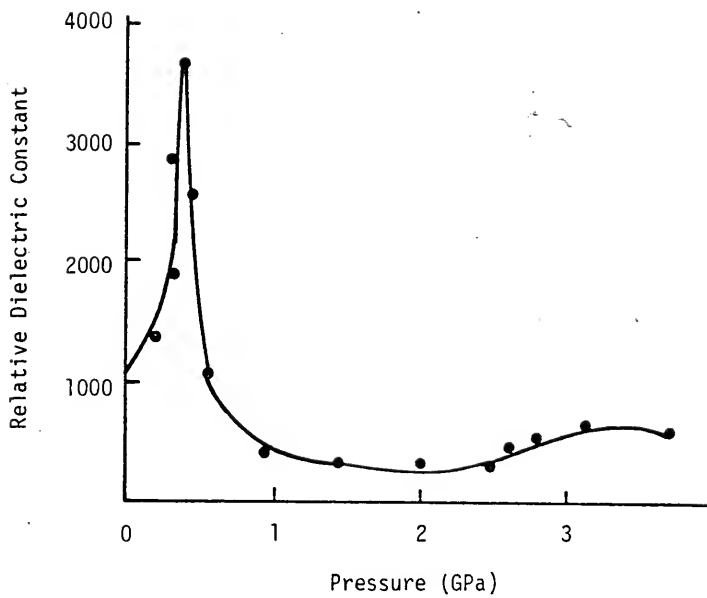
Figure 19. Relative dielectric constant versus pressure for PZT 95/5 ferroelectric ceramic. The dielectric constant was determined by measuring the slope of the poling curve.
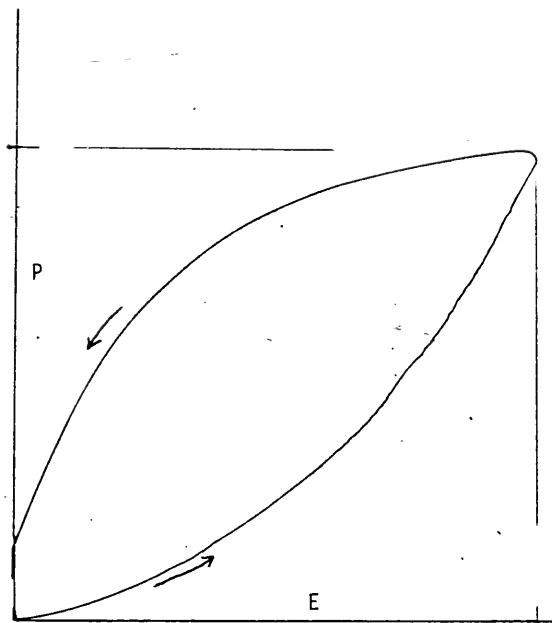
Figure 20. A typical polarization versus pressure poling trace
near the FE-AFE transition. This curve illustrates
the "lossiness" of the sample near the transition.

A dielectric anomaly, which at first was thought to be a phase change, is shown in the high pressure regions of Figures 14 and 19. Based on an average of six runs, the pressure at which this occurred was 2.25 $\pm$ 0.15 GPa.

This effect is believed to be associated with pore collapse in the ceramic. Similar results were noted by Polandov et al. (25) as mentioned in section 2.4. Also (as mentioned previously), the two wave patterns noted in shock experiments on ferroelectrics may be associated with this phenomenon.

The effect is irreversible in that it is not encountered during the pressure release cycle or on subsequent pressurization cycles. The sample was too small to determine density changes prior to and after pressurization. Electron microscopy of a sample which had been subjected to pressures above where the effect was noted was attempted but the sample fell apart during polishing and replicating, suggesting that compaction, which caused fragmentation of the specimen, occurred. This fragmentation was also observed on a sample that was retrieved for retest after it had been "compacted." A lead was missing and an attempt was made to re-ball bond another lead in place; however, the sample was easily crushed under the force of the ball bonding anvil.

Loops performed on a compacted sample at zero pressure did not resemble those on a zero pressure

noncompacted sample; they appeared like the noncompacted
sample loop near the transition region, i.e., similar to
the loop shown in Figure 18.

In some cases, the variation in K was sharp and in
others it was gradual as shown in Figures 14 and 19. The
dielectric constant change that occurred ranged between
10 and 30.

4.2 Low Pressure Dielectric Characteristics

The small signal dielectric constant at 1 kHz was
used to examine a variety of pressurization processes up
to and slightly beyond the FE-AFE transition. The initial
series of tests consisted of measuring the 1 kHz dielectric
constant before and after looping at each pressure interval.
The results (see Figure 21) show that at each interval
up to the transition the dielectric constant increases
after looping while at pressures greater than the transi-
tion, the dielectric constant decreases after looping. In
Figure 21, it is observed that the dielectric constant
varies only slightly between successive pressure intervals
which might suggest that there may be only a small change
in dielectric constant if the sample were not looped at
each pressure interval; however, when K was measured with-
out successive looping it still gradually rose (see Figure
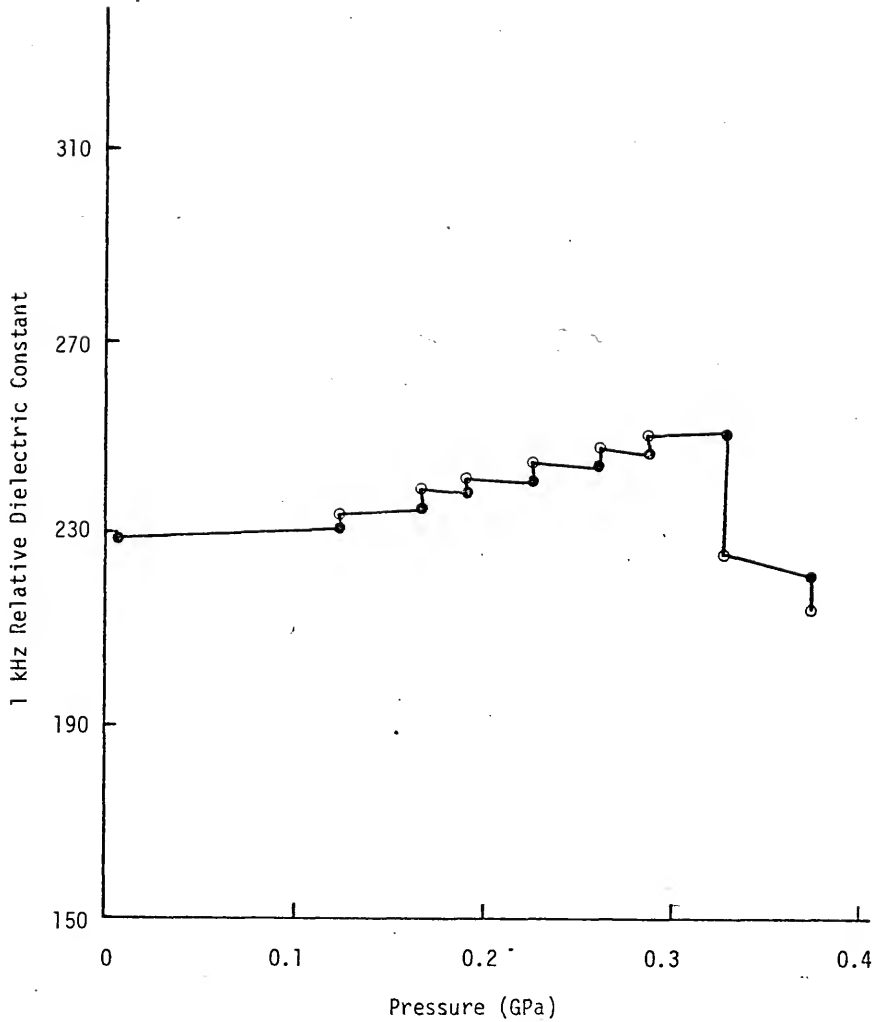22) at a rate that exceeded that of Figure 21. When not

Figure 21. 1 kHz small signal relative dielectric versus pressure for PZT 95/5 ferroelectric ceramic. Measurements were made before (solid dots) and after (circles) looping.

looped the phase transition occurred at 0.4 GPa or approximately 0.11 GPa higher than when the sample was looped at each pressure interval. These results, as do those in Figure 18, show that looping provides activation energy that induces a portion of the AFE phase. In so doing, the net dielectric constant is lower as shown in Figure 22, but there is still an increase in K after looping as seen in Figure 21.

The variation of dielectric constant for a sample initially at 0.5 GPa (in the AFE phase) as pressure is released is shown in Figure 23. Looping was not performed at each pressure interval; depressurization was stopped long enough for the pressure to stabilize and a dielectric measurement to be made. When pressure was reapplied (again without looping between each measurement), the curve shown by the dashed line in Figure 23 was followed. From the depressurization curve it is apparent that without looping, the AFE to FE transition is quite sluggish. It is interesting that when pressure is reapplied, a peak in K is encountered at approximately 0.19 GPa.

Figures 21, 22, and 23 illustrate the dependence of the dielectric response on the degree of polarization. Based on the limited testing that was performed in this sequence, it appears that a model describing the variation of low pressure dielectric properties with electric field may be quite difficult.
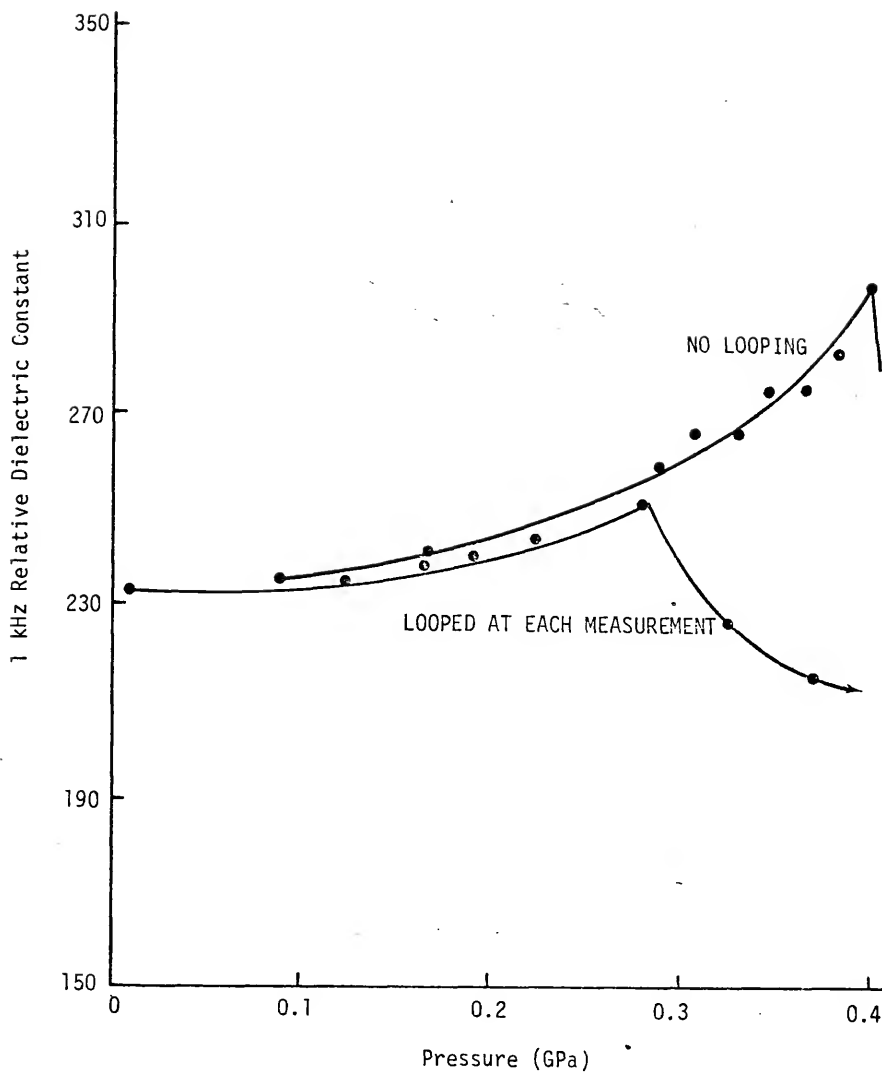
Figure 22. 1 kHz relative dielectric constant versus pressure for PZT 95/5 ferroelectric ceramic. The lower plot is taken from Figure 21 and shows K when the sample was looped at each measurement. Looping was not performed during the testing for the upper plot.
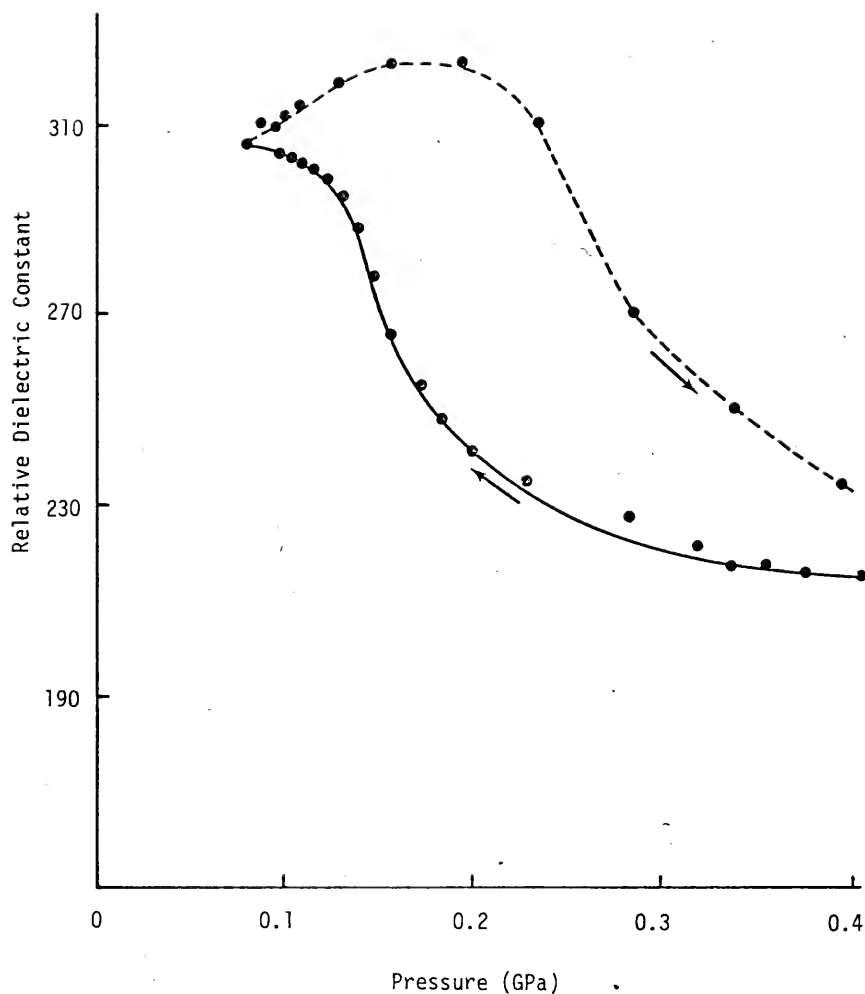
Figure 23. 1 kHz relative dielectric constant versus pressure of PZT 95/5 ferroelectric ceramic. Testing was initiated when the sample was at 0.5 GPa in the AFE state. The sample was depressurized and repressurized. Looping was not performed between measurements.

4.3   Curie-Weiss-Like Behavior

In section 2.4 it was mentioned that at constant
temperature the static dielectric constant of $BaTiO_3$,
$PbTiO_3$, and $SrTiO_3$ in the nonpolar FE phase obeys a Curie-
Weiss-like relationship. In connection with the present
study, it was questioned whether or not PZT 95/5 would
follow a similar pattern in the AFE phase. Since the high
voltage dielectric characteristics of PZT 95/5 were of
greatest interest, practically all of the small signal
data were taken prior to or following looping of the sample.
As pointed out in section 4.2, looping at pressures near
the transition induces the AFE phase and as a consequence,
the small signal dielectric constant is not as large as
that determined if looping had not been performed. How-
ever, in one run the 1 kHz dielectric constant was mea-
sured without intervening looping. Part of the results
of this test is shown in Figure 22. The variation of
dielectric constant with pressure in the AFE phase is
shown in Figure 24. An attempt was made to fit these
data to a Curie-Weiss-like relationship similar to the
method used by Samara (21) in fitting $BaTiO_3$ data.

By extrapolation of 1/K to zero when plotted against
p it is possible to find p_0. This was determined to be
0.34 GPa (refer to Figure 24). With this value a plot of
K versus $1/(p-p_0)$ was constructed. The results (shown in
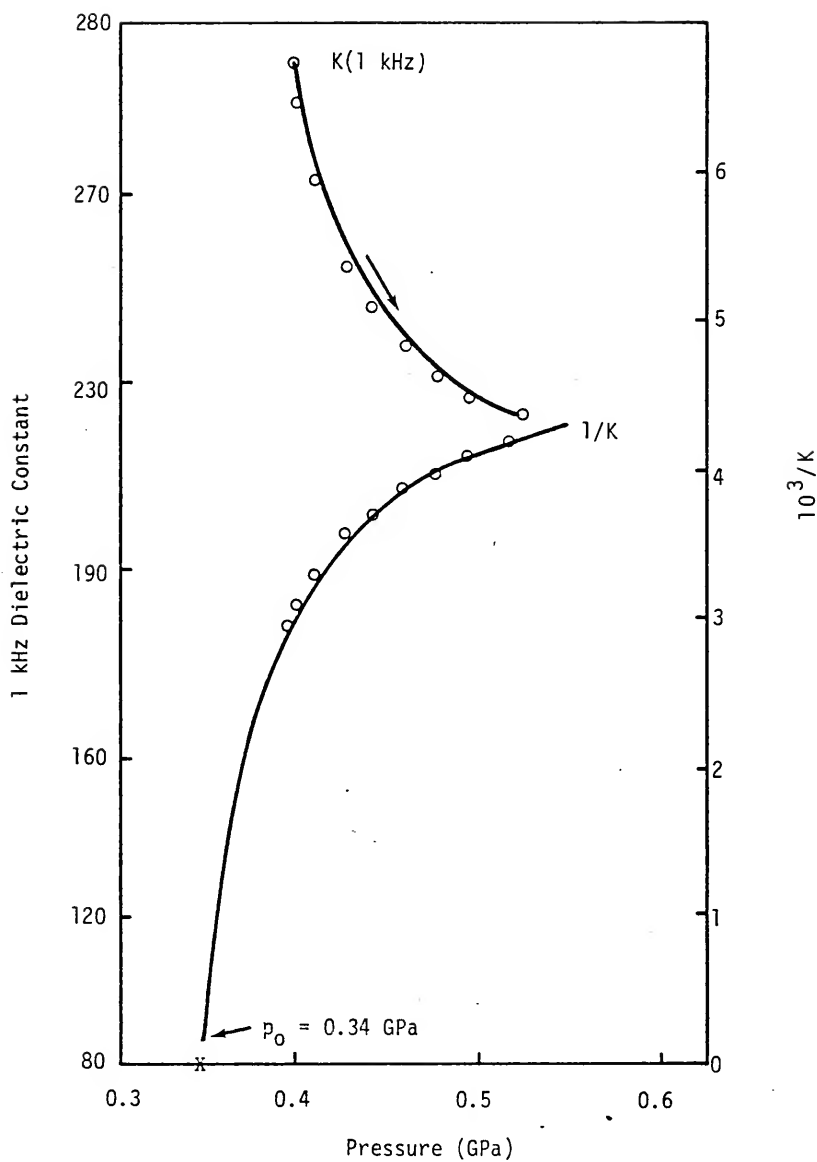Figure 25) indicate that the relationship is linear;

Figure 24. Pressure versus 1 kHz dielectric constant in the AFE phase for PZT 95/5 ceramic. The reciprocal dielectric constant is plotted to determine p_o.
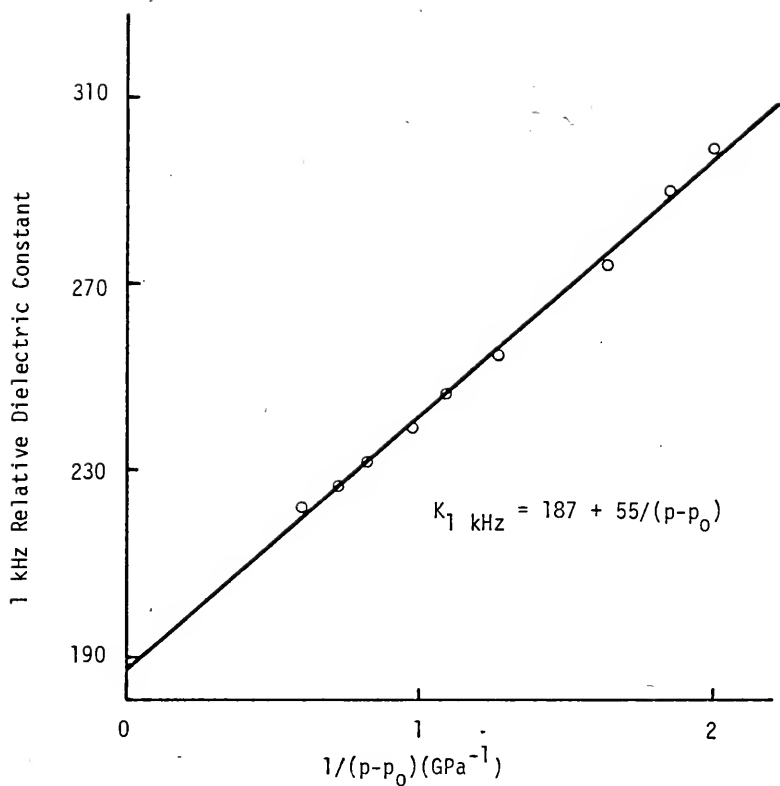
Figure 25. 1 kHz relative dielectric constant versus $1/(p-p_O)$ demonstrating that a Curie-Weiss-like relationship is followed for this ceramic in the AFE phase. For these calculations $p_O = 0.34$ GPa. The resulting relationship is shown on the illustration.

however, instead of fitting a single term Curie-Weiss-like
equation, an additional term corresponding to the y inter-
cept was necessary. For this sample, the resulting Curie-
Weiss-like relationship was found to be

$$K = 187 + 55/(p - p_o) \quad .$$
(4.2.1)

In the nonpolar PE phase, Samara (10, 21, 22, and
23) was able to demonstrate an excellent fit of the data
to a single term equation. The test procedure and composi-
tions resulted in a much greater increase in dielectric
constant at the transition than was determined in the
present study. If a smaller pressure interval had been
selected between measurements, a larger dielectric con-
stant peak at the transition (and thus greater accuracy)
would have resulted. Another difference was that Samara
examined the static dielectric constant while this study
used the 1 kHz relative dielectric constant. As will be
shown in the next section, the two values are nearly the
same in this pressure range.

It was of interest to examine data in which loop-
ing (or poling) was performed at each measurement interval.
Figure 26 is a graph of three tests in which 1/K versus
pressure was plotted to determine p_o. It is seen from the
extrapolation of data from test run #8 that p_o could en-
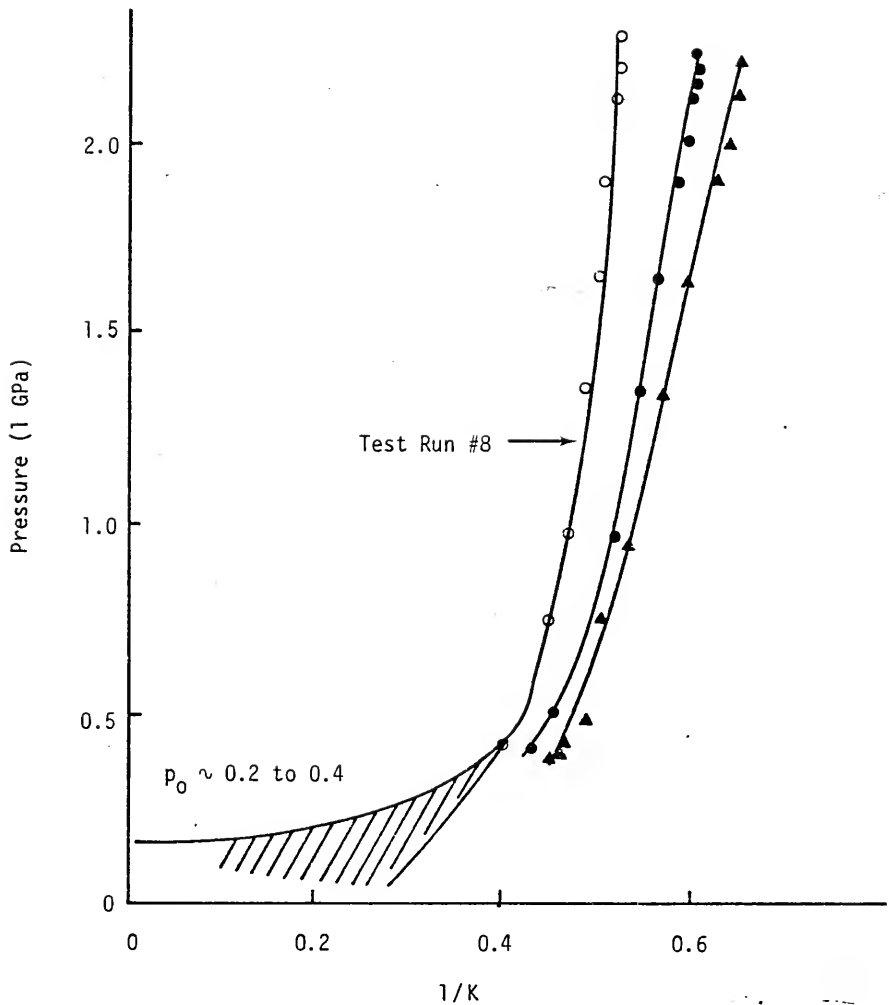compass a range of values. Graphs of dielectric constant

Figure 26. Pressure versus the reciprocal of the 1 kHz relative dielectric constant for high pressure examinations of three PZT 95/5 ceramic samples. The samples were looped between each measurement.

versus $1/(p-p_0)$ for values of p_0 ranging from -0.4 to 0.2 GPa are shown in Figure 27. A linear fit of the data appears to be possible at pressures near the transition but deviates at higher pressures. For this sample, as p_0 decreases linearity increases. It is evident that Curie-Weiss-like relationships are quite dependent on p_0; thus, it is mandatory that care be exercised in gathering experimental data about the transition so that the peak value of dielectric constant can be determined. This would increase the accuracy with which p_0 could be determined.

4.4 Frequency Dependent Behavior

As mentioned previously, small signal measurements consisted of determining the dielectric constant and dissipation factor at 1 kHz, 10 kHz, 100 kHz and 1 MHz. With these data, it is possible to determine the imaginary components of the complex dielectric constant at various frequencies and if a sufficiently wide range of frequency is available, dielectric relaxation characteristics can be determined. Table 1 is a listing of the complex dielectric constant components of PZT 95/5 determined on a typical pressurization run. For conciseness only a part of the results is shown in the table.

At a particular pressure, the components of the complex dielectric constant were determined (as explained
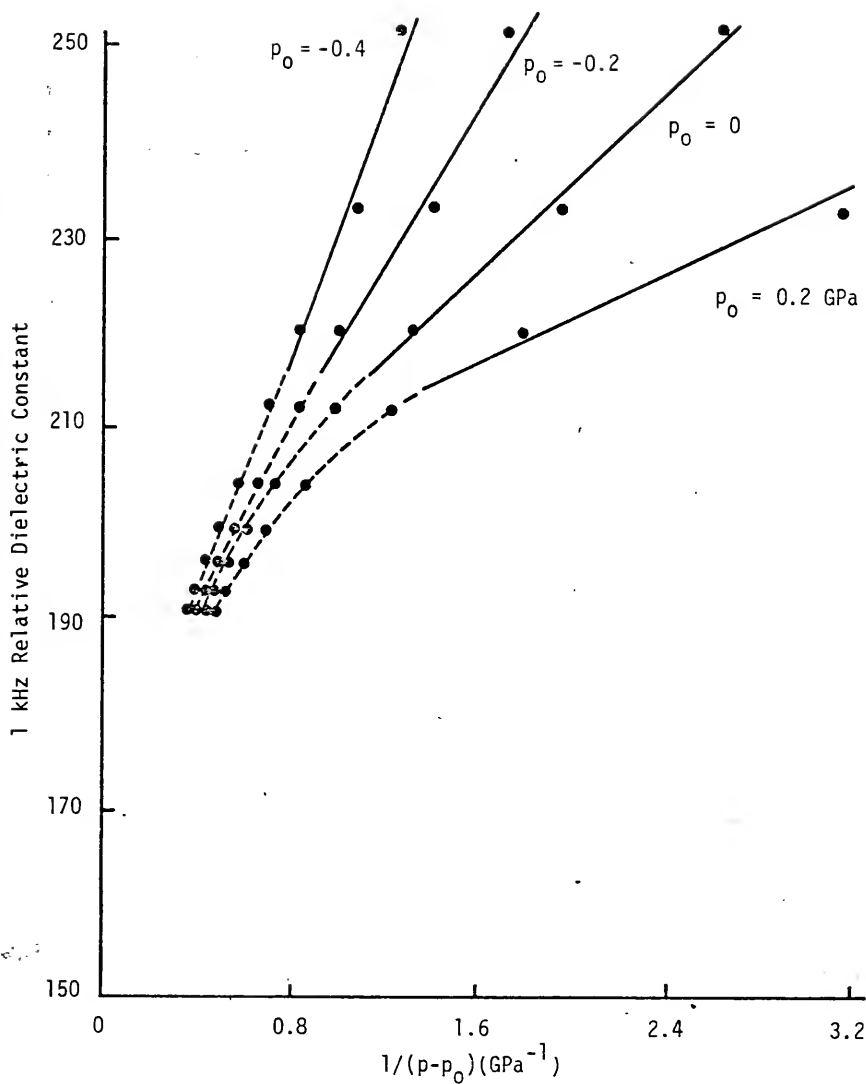
Figure 27. 1 kHz relative dielectric constant versus $1/(p-p_o)$ for PZT 95/5 ceramic. Four values of p_o were examined in conjunction with the data from test run #8 in Figure 26 to determine how p_o affected linearity.

Table 1

Real and imaginary complex dielectric constant components of PZT 95/5 ferroelectric ceramic when tested at four test frequencies at pressures up to 3.67 GPa

| Pressure GPa | Relative Dielectric Constant at Specified Frequency | | | | | | | |
| | 1 kHz | | 10 kHz | | 100 kHz | | 1 MHz | |
	$\varepsilon'/\varepsilon_0$	$\varepsilon''/\varepsilon_0$	$\varepsilon'/\varepsilon_0$	$\varepsilon''/\varepsilon_0$	$\varepsilon'/\varepsilon_0$	$\varepsilon''/\varepsilon_0$	$\varepsilon'/\varepsilon_0$	$\varepsilon''/\varepsilon_0$
0.069	322	7.56	309	7.12	299	7.56	291	10.2
0.302	355	9.19	338	8.76	325	9.21	315	12.7
0.384	358	9.55	341	8.95	328	9.42	.317	13.2
0.411	334	3.73	326	4.86	319	5.30	313	7.02
0.506	289	1.82	284	3.32	279	3.69	275	5.07
0.964	257	0.616	254	1.28	251	2.31	250	3.62
01.64	242	0.096	241	1.74	237	1.94	236	2.80
2.12	226	0.0	224	1.52	222	1.77	220	2.53
2.50	234	0.91	231	2.38	227	2.64	225	3.71
2.95	251	1.93	246	3.57	241	3.95	236	5.06
3.67	248	1.78	243	3.52	238	3.90	233	5.19

in section 2.1) and plotted on a complex plane. Figure
28 shows graphical representations of K' and K" at selected
pressures. The plots at 0.089 and 0.384 GPa represent the
dielectric character of a poled ferroelectric below the
transition. The concave upward curvature does not resemble
any of the common relaxation models described in section
3.2, although the data may fit some of the other models
described in reference 8. After the FE-AFE transition
the curvature is such that if extrapolated to the real
axis it would be possible to obtain the static dielectric
constant, K_s. After the pressure is increased past 1.64
GPa, the curve becomes concave downward and resembles the
distributive relaxation time model described in section
2.1.

From the data used to construct Figure 28 at
pressures of 1.64 GPa and above, it may be possible to
determine the instantaneous dielectric constant, K_i, if
the distributive relaxation time model is assumed. After
an examination of this possibility, it was decided not
to continue for the present study. The reason is due
to the fact that it is felt that the resulting value of
ε_i would contain such a large degree of uncertainty that
it would not be of any value and would possibly be mis-
leading in shock depolarization studies. It is felt that
to obtain this information, additional testing in a higher
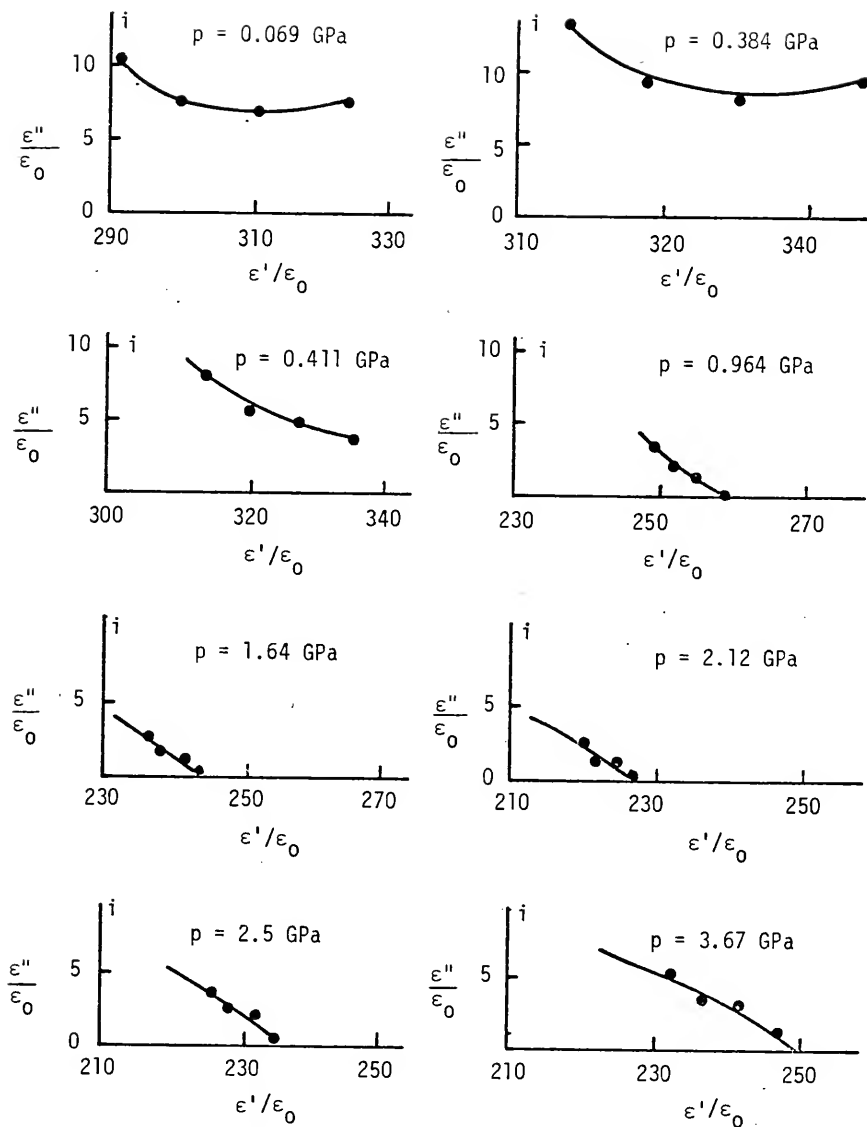frequency range should be performed.

72

Figure 28. Components of complex dielectric constant (K' and K")
plotted on complex plane at various pressures. The static
dielectric constant K_s is location at which plot extrapo-
lates to real axis.

CHAPTER 5

SUMMARY AND CONCLUSIONS

Electrical measurements pertinent to the dielectric characterization of PZT 95/5 ferroelectric ceramic were determined as a function of pressure up to 4 GPa. A 600/2400 tetrahedral anvil apparatus was used to attain the pressures desired. This required development of a test fixture which could subject the specimen to truly hydrostatic pressures and high voltages. An accurate measurement of the pressure was made using a manganin wire pressure transducer.

The purpose of the study was to establish dielectrical data which could be applied to shock depolarization models. Low signal dielectric constant results as well as high voltage poling dielectric results were determined as a function of pressure. These data have direct application to some of the simpler shock depolarization models. More refined models require knolwedge of the dispersion and relaxation characteristics of the dielectric. Specifically, it is desired that the dielectric constant be specified over a frequency range between the static and instantaneous dielectric constant. It was found that at high pressures when the components of the complex dielectric

73

constant were plotted, the data resembled a distributive relaxation time model near the static dielectric constant. However, it is not feasible to calculate an instantaneous dielectric constant because of the large extrapolation error. To obtain these data, an investigation at higher frequencies is needed.

Based on small signal dielectric measurements with no looping, the FE-AFE transition was located at 0.4 GPa. When the sample was looped at each pressurization interval, the transition pressure was lower (it averaged 0.32 GPa). The electric field induces and stabilizes a portion of the AFE state while the material is considered to be in the FE phase.

Due to the fact that one of the intentions of this program was to establish high voltage characteristics of PZT 95/5 with pressure, only one test was performed when small signal data with no intervening looping was performed. However, the data in the AFE phase immediately following the transition were found to fit a Curie-Weiss-like relationship.

An effect at high pressures was observed. This was thought to be a phase change but due to the fact that it was irreversible as well as the fact that the material was easily fragmented, it is concluded that the effect is attributed to collapse of pores in the ceramic. Similar results were reported by Russian experimenters (25).

Except for a study by Berlincourt and Krueger (18) which examined low signal dielectric properties of PZT 95/5 up to 0.5 GPA, to the author's knowledge the present work represents the only study of PZT 95/5 at high voltages and high pressures. It is believed that the data will be an important contribution to shock depolarization modeling and to the understanding of PZT 95/5 at high pressures.

APPENDICES

APPENDIX A

TETRAHEDRAL PRESS DESCRIPTION AND OPERATION

For the 600/2400 tetrahedral anvil apparatus used
in this study, the rams were made up of an anvil assembly
mounted on a 30.5-cm dia. piston. The anvil consisted of
a 4.76-cm dia. cemented tungsten carbide cylinder having
an equilateral triangular face with an edge length of
3.18 cm.

A diaphragm air pump in the control console was
used to pressurize the hydraulic oil which in turn drove
the rams. Mounted on the control console was a 0- to
1100-psi Heise gage that indicated the hydraulic oil
pressure. The face of this gage was incremented in 100-
psi intervals and was readable to the nearest 10 to 15 psi.

The operation of the presses of this nature is not
complex. The most critical item concerns the initial
adjustments of the drawback mechanisms and the pressure
release cycle which, if performed too rapidly, results in
a specimen "blowout." With the tetrahedral press, once
pressure is applied, the operator has little control except
for the rate of pressurization. A schematic of the pres-
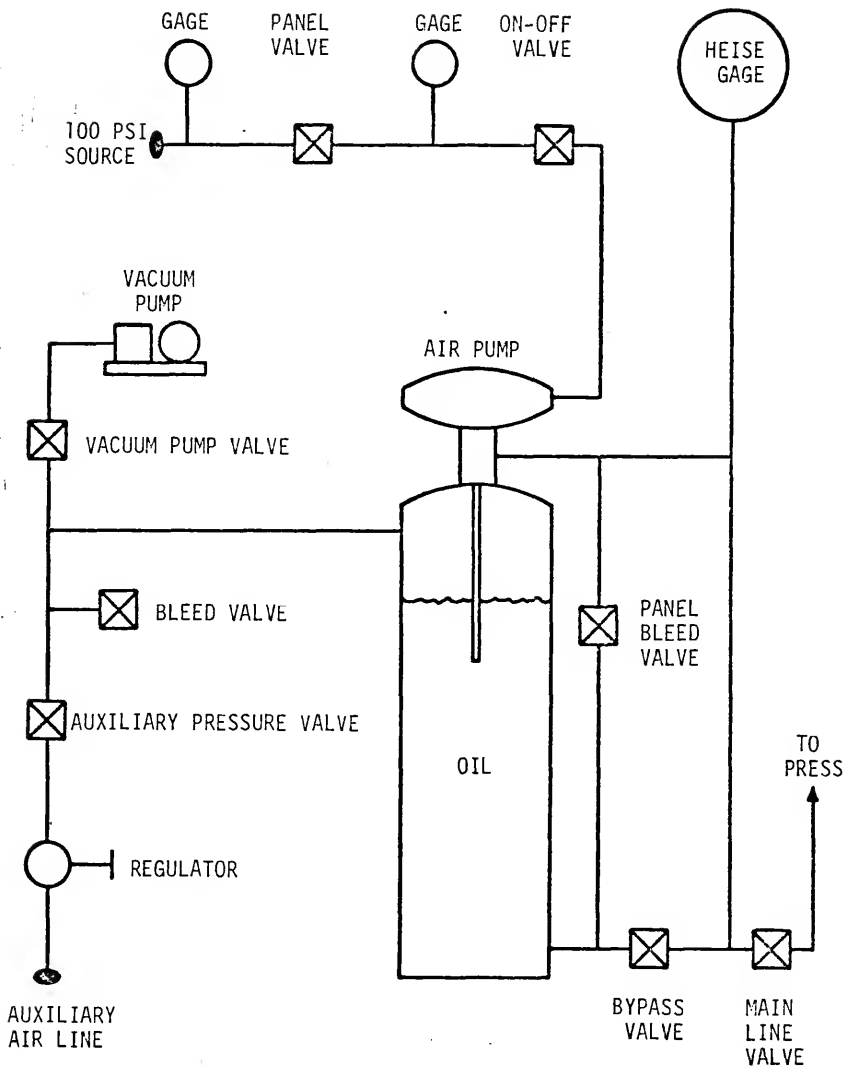surization system is shown in Figure A-1.

Figure A-1. Schematic of tetrahedral anvil apparatus pressurization system.

On the back side of the platens of these presses
are hand-operated devices called drawback mechanisms which
retract the rams once they have been extended. To aid in
ram retraction, the intake line of a vacuum pump was plumbed
into the top of the oil reservoir. A partial vacuum on the
hydraulic oil would draw oil from the four cylinder cavities
and retract the rams. In like fashion, to extend the pis-
tons, the oil reservoir was pressurized to as much as 200
kPa with air. These adaptions eliminated a large part of
the effort and time required to manipulate the drawback
mechanisms.

The steps taken in the initial adjustment of the
anvils as well as the steps taken to operate the press are
outlined below. Two preliminary procedures describing how
the rams are retracted and advanced are given.

Advancement of Rams (refer to Figure A-1)

1. Close vacuum pump valve.
2. Open auxiliary pressure line valve, main
   line valve, bypass valve, and panel valve.
3. Adjust drawback mechanism.
4. Adjust regulator on auxiliary pressure line
   to 15-30 psig depending on ram advance rate
   desired. (The ram advancement can be stopped
   at any position by adjustment of the drawback
   mechanisms.)

Retraction of Rams (refer to Figure A-1)

1. Close auxiliary pressure line valve.

2. Open vacuum pump valve, main line valve, by-pass valve, and panel valve.

3. Adjust drawback mechanism.

4. Start vacuum pump. (Ram retraction can be stopped at any position by adjustment of the drawback mechanisms.)

Alignment of Anvils (refer to Figure A-1)

1. With top platen removed, adjust each lower ram until piston face is flush with platen face.

2. Advance rams until the three anvils are close to touching. (It is desired that rams can be positioned such that anvil edges when touching will form a "nest.")

3. Adjust the anvil assembly position by rotating the two eccentric adjusting rings between the anvil assembly and piston. (By making these adjustments and advancing or retracting the rams, it is possible to form the nest.)

4. Retract rams and align piston faces flush with platens.

5. Advance rams until the nest is formed. Note the exact number of turns on the drawback

mechanisms required to form the nest. (For
the present study the turns were 18 for #1
ram, 11 for #2 ram, and 7 for #3 ram.)

6. Position top platen and replace hinge pins.
    Connect ram #4 hydraulic line. To accomplish
    this it may be necessary to retract the rams
    of the lower platens.

7. Advance lower rams to form nest (if not already).
    Lower top ram and adjust anvil assembly using
    eccentric adjusting rings. By careful adjust-
    ments it is possible to close the tetrahedral
    nest. (Visual access is limited; thus, an
    indirect method such as attempting to hold
    the gap between the anvil binding rings uni-
    form can be used as a possible alignment
    method.)

Pressurization Cycle (refer to Figure A-1)

1. Position pistons of lower rams flush with
    platen faces.

2. Place pyrophyllite tetrahedron in press.
    (The top ram should be withdrawn sufficiently
    from the previous run to allow the tetrahedron
    to slip into place.)

3. Support tetrahedron so that it is not locked
    in place by the lower anvils. (For this

study the support consisted of a 3.1-mm dia. copper wire bent into a U-shape approximately 50 cm on a side.)

4. Adjust drawback mechanisms of the lower rams so that when extended they will be within 2 or 3 turns of nest position.

5. Adjust air regulator of auxiliary pressure to 25-30 psig.

6. When two of the three drawback mechanisms tighten, remove tetrahedron support mechanism and advance the top ram. Check to be sure electrical leads are properly located and not wedged between two anvils.

7. When drawback mechanisms on all lower platens are tight and the top anvil is close to the tetrahedron, reduce regulator pressure of auxiliary air to 10 psi. (Additional adjustments of the drawback mechanisms of the lower rams may be required.)

8. When the top anvil contacts specimen, reverse drawback mechanism until tight. (Anvil-tetrahedron contact for the top ram is difficult to determine. The present study relied on operator judgment of the gap between binding rings. The possibility of using a thin wire between the tetrahedron and anvil was

examined, i.e., anvil closure occurred when the wire was wedged. Too much force by the top anvil at this stage is detrimental because it will cause the lower anvils to retract.)

9. Immediately turn auxiliary air supply off and bleed to atmosphere.

10. Tighten bypass valve and panel valve.

11. Check test sample instrumentation.

12. Start press air pump and pressurize until Heise gage reads 10 to 20 psi.

13. Advance all drawback mechanisms 10 turns.

14. Place protection covers in place.

15. Continue pressing.

Depressurization Cycle (refer to Figure A-1)

1. If at high pressure (over 1000 psi on the Heise), slowly lower pressure using panel valve. (For these tests it was found that a 100-psi drop in 20 sec was a sufficiently slow rate to prevent specimen blowout).

2. When at (or close to) 0 psi on the Heise gage, remove protection covers and retract rams.

3. By adjusting drawback mechanisms, stop rams of lower platens when each piston face is flush with platen face. (It is possible to accomplish this without operator attention by

proper adjustment of drawback mechanisms. For
this study it was found that by advancing the
#1, #2, and #3 drawback mechanisms 3, 4, and
11 revolutions, the rams would withdraw to the
correct position.)

4. The top ram should be retracted more than just
   the amount required to remove the pressed
   tetrahedron; space should be allowed to fit
   the tetrahedron for the next test. (For this
   study the extraction of the tetrahedron was
   performed using a 50-cm long, 3.2-mm dia.
   steel wire having a 90° bend at one end with
   a 3-cm leg.)

5. Turn vacuum pump off.

APPENDIX B
FABRICATION OF TETRAHEDRON

The pyrophyllite used for these studies was in the form of 30.6-cm-long prisms having a triangular cross-section. Two legs of the triangle were 4.4-cm long while the other was 5.2 cm. Each prism was cut into 6 equal pieces by sectioning perpendicular to the axis at 5-cm intervals. Using Crystalbond 509 ®* thermoplastic cement, which flows at approximately 135°C, a 1.5-cm dia. by 6-cm-long steel rod was bonded to the largest rectangular face of each piece as shown in Figure B-1.

This assembly was then placed in an indexing tool mounted at the appropriate angle on the bed of a milling machine. The faces of the tetrahedron were fabricated until an edge length of 39.75 ± .13 mm was obtained by rotating the indexing head by 120° intervals and feeding the pyrophyllite into a vertical milling tool.

After the tetrahedron was removed from the steel rod, the following steps were taken to fabricate the test sample cavity:

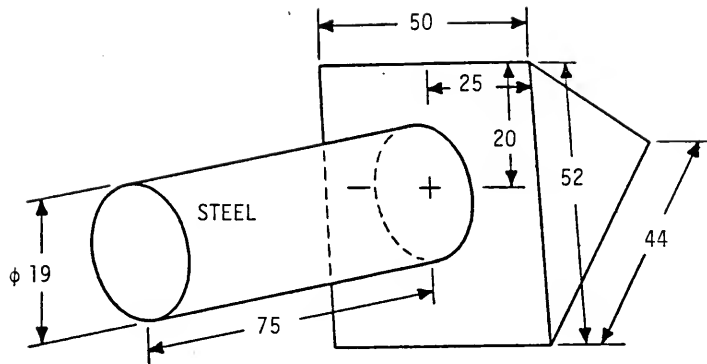*Aremco Products, Inc., Ossining, N. Y.

Figure B-1. Location of steel holding rod on pyrophyllite prism. The attachment is made using a thermoplastic adhesive which melts at approximately 135° C. This assembly is positioned in a milling machine and the pyrophyllite is shaped into a tetrahedron. Dimensions in mm.

1. Using Crystalbond 509 $^{\circledR}$, the tetrahedron was
   mounted on a 32 x 32 x 6.4-mm steel plate having
   a 12.7-mm dia. hole. The hole location as well
   as tetrahedral position (in dashed lines) is
   shown in Figure B-2.

2. The apex of the tetrahedron mounted on the steel
   plate was ground flat using a 600 grit diamond
   wheel. (This left a small triangular face on
   which the center could be pinpointed to start
   a pilot drill for step 3.)

3. A hole was drilled at the center of this tri-
   angle using a 0.18-mm dia. drill.

4. Using this hole as a pilot, a larger hole
   (its size depends on the number of electrical
   leads required) was drilled into the tetrahedron
   9.53-mm deep. (Care was taken in drilling
   pyrophyllite; it appeared to be nonuniform in
   hardness and small drill bits were easily
   broken.)

5. The assembly was placed in a wafering machine
   (see Figure B-3) and the apex tetrahedron was
   removed using a 15.2-cm dia. by 0.5-mm thick
   600 grit diamond blade.

6. The apex tetrahedron was then hardened by
   heating to approximately 975° C and holding
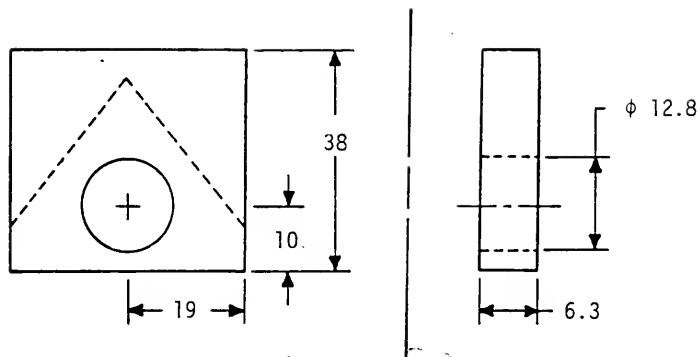   at the peak temperature for 20 min. The heat-up

Figure B-2. Configuration of backup plate used to hold tetrahedron for fabrication of test specimen cavity. Dimensions in mm.
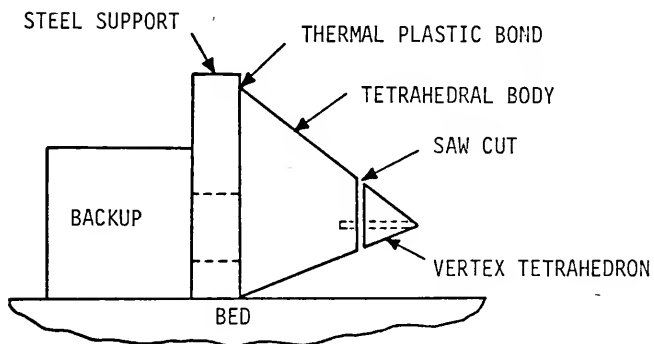

Figure B-3. Position of tetrahedron support assembly on bed of wafering machine.

rate was approximately 8° C/min. (This process, when performed in air, changed the color of pyrophyllite from grey to pink. When performed in an inert atmosphere, the color remained grey but the prophyllite appeared to have transformed to the same hardness.)

7. With the bulk of the tetrahedron still mounted on the steel plate, a 6.35-mm dia. hole was drilled through the tetrahedron using the center of the equilateral triangle left by the apex tetrahedron as the starting position. The truncated tetrahedron was removed from the steel plate.

8. Because of the 0.5-mm saw blade gap left when the apex tetrahedron was removed, it was necessary to fill this space with a 0.5-mm-thick pyrophyllite spacer. A triangular shaped 0.5-mm-thick slab was bonded to the truncated tetrahedron using an epoxy adhesive. The 6.35-mm dia. hole was extended through the shim and then reamed using a size "G" (6.477-mm dia.) drill. The edges of the shim were filed flush with the edges of the tetrahedron.

9. The apex tetrahedron and truncated tetrahedron were ultrasonically cleaned in acetone and then dried at 200°C. These parts were stored in a desiccated cabinet until ready to use.

APPENDIX C

CONSTRUCTION OF THE MANGANIN CELL

Manganin wire can be obtained with either enamel or cloth (silk or cotton) electrical insulation. Initially it was believed that the cloth insulation was preferable because of the possible loss in accuracy resulting from the structural support provided by enamel. However, when cloth-insulated manganin was evaluated, it was found that the dielectric fluid media used became conductive in the high electric fields. This was apparently due to a transfer of contaminants from the cloth to the fluid. As a consequence, it was necessary to consider enameled manganin wire.

The initial series of tests on enameled manganin were run using 0.0355-mm-dia. wire with a resistance of 3.94 ohms/cm.* Several test cells consisting of 25- to 30-cm lengths of this manganin wire wound on plastic bobbins were fabricated and evaluated in the tetrahedral press. The resistance response of the manganin with pressure was substantially out of line with the reported characteristics

---

*This manganin was manufactured by W. B. Harris, Newark, N. J.

90

of Manganin (42). On subsequent runs a larger size, 0.0799-mm-dia. enameled manganin wire, was used.* Details concerning the calibration of this wire are given in Appendix H.

The manganin wire was wound on a polyethylene bobbin which for high pressure studies was preferred over Teflon ® ** (which was used initially) because of the 0.54 GPa phase transition inherent in the latter. The bobbin not only provided support for the wire but also pro-vided an alignment and lead separation mechanism for the ferroelectric sample lead wires. A stereomicroscope was used as an aid throughout the assembly of the cell. The steps followed in the construction of the manganin pressure cell are as follows:

1. A bobbin was fabricated to the dimensions shown in Figure C-1 from 6.35-mm-dia. poly-ethylene rod.

2. A thin layer of Crystalbond 509 ® was placed on the mid-portion of the bobbin by heating the bobbin and Crystalbond 509 ® to 250° C and using a small diameter wire to spread and adjust to the correct amount.

3. A 3-cm length of wire (No. 28 magnet wire) was

---

*Obtained from I. Fritz, Sandia Laboratories, Albuquerque, N. M.

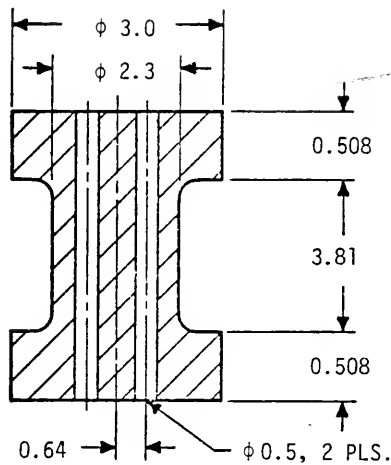**E. I. duPont de Nemours & Co., Wilmington, Del.

Figure C-1.   Configuration of polyethylene bobbin used to support
manganin wire. Two center holes are used to guide leads
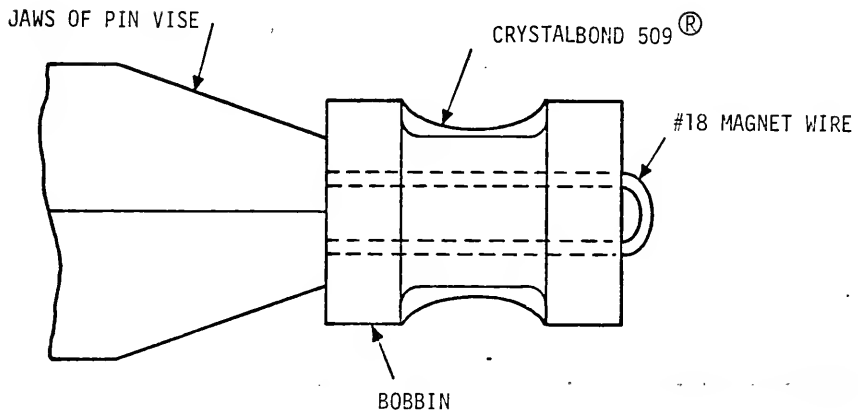to the FE sample. Dimensions in mm.

Figure C-2.   Positioning of bobbin in pin vise in preparation for
winding manganin wire. Crystalbond 509® thermoplastic
adhesive which is later dissolved away separates the
manganin from the bobbin so the wire is floating.

fed through the holes of the bobbin as shown
in Figure C-2. The ends of the wire were clamped
in the jaws of a pin vise.

4. Four 0.018-mm-dia. holes were drilled into
the bobbin as shown in Figure C-3.

5. A 35- to 40-cm length of manganin wire was
measured and one end was fed into two of the
four holes (as shown in Figure C-4), leaving
a 3-cm-long leader.

6. By placing the pin vise in a lathe and rotating
it at a slow speed, the manganin was uniformly
wound on the bobbin. This was a manual opera-
tion in which the wire was kept taut by holding
it in a thin-cotton-gloved hand. When com-
pleted, the free end was fed into the two
remaining 0.018-mm-dia. holes.

7. The cell was removed from the pin vise and the
two leads of the manganin wire were stripped
of enamel to within 1-3 mm of the bobbin using
Epoxystrip ®.* This required great care;
tweezers and cotton swabs were used.

8. The magnet wire was removed and the cell was
ultrasonically cleaned in acetone. During this

---

*Beck Chem., Cleveland, Ohio.
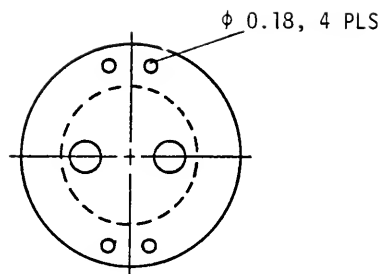
ϕ 0.18, 4 PLS

Figure C-3. Location of 0.18-mm-dia. holes in bobbin. The holes provide a mechanism by which the manganin can be held to bobbin. Dimensions in mm.

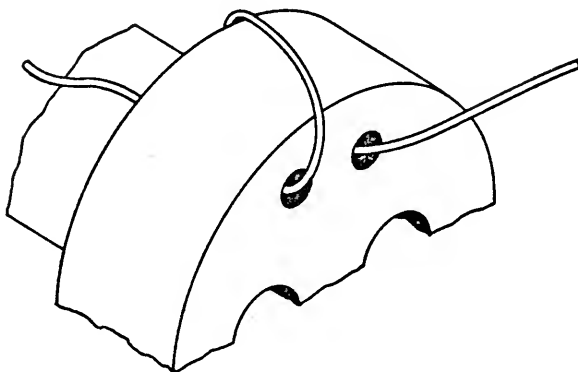

Figure C-4. Method of holding manganin wire to bobbin by feeding through two 0.18-mm-dia. holes.

cleaning, the Crystalbond 509 ® about the
bobbin dissolved, allowing the coiled manganin
wire to remain suspended from the bobbin.

APPENDIX D

FERROELECTRIC SAMPLES

Atmospheric fired ceramics having a density of approximately 7.6 gm/cc were used for these studies. This material was manufactured* using the slip cast process and was available in 1.2-mm-thick rectangular-shaped slabs which were ground to a thickness of approximately 0.4 mm using a 600 grit diamond wheel. The ground slab was cleaned and both sides were electroded using the sputter deposition technique. This process consisted of cleaning in an ion beam and then depositing approximately 4 μ of chrome followed by 16 μ of gold. Rectangular test samples measuring approximately 1.5 x 3.5 mm were then fabricated using a wafering machine.

Gold lead wires approximately 1-cm long and 0.16-mm diameter were thermal compression bonded to the electroded surface using a Hughes ball bonding device.** It was necessary to stagger the lead location so that the portion

---

*Gulton Ind., Santa Barbara, Calif.

**Hughes Aircraft, Oceanside, Calif.

of the specimen directly under the joint could support the force of the ball bonding tip. Gold lead wires smaller in diameter could have been used; however, these electrical leads also provided structural support for the sample. After ultrasonically cleaning in acetone and vacuum drying, all the specimens were tested by running a hysteresis loop.

Due to the excessive amount of specimen breakage which occurred during the experiment, material from six different lots of ferroelectric ceramics was used.

APPENDIX E

FABRICATION OF CAPSULE, PLUGS AND LEAD WIRES

The capsule used to contain the specimen, manganin cell and dielectric fluid was fabricated from 6.35-mm O.D. 304 stainless steel tubing having a wall thickness of 0.152 mm. After cutting to a length of 20.3 mm, the capsule was deburred with a 127-mm-dia. aluminum oxide mounted pointed wheel grinder. It was possible to deburr and slightly taper the ends of the tubing using this grinder. A cross-sectional view of the resulting capsule is shown in Figure E-1.

Polyethylene plugs fabricated as shown in Figure E-2 were used to contain the fluid in the cell. Holes were drilled in the bottom plug in order to feed the electrical lead wires into the cell. Electrical feedthrough constituted one of the major obstacles in this program. Numerous configurations were attempted. Initially uninsulated wire was used in conjunction with the cell configuration shown in Figure 9. Studies were performed in which leads were brought out through the tetrahedral vertex as well as through the pyrophyllite gaskets. In most cases the lead wires not only frequently sheared off but when
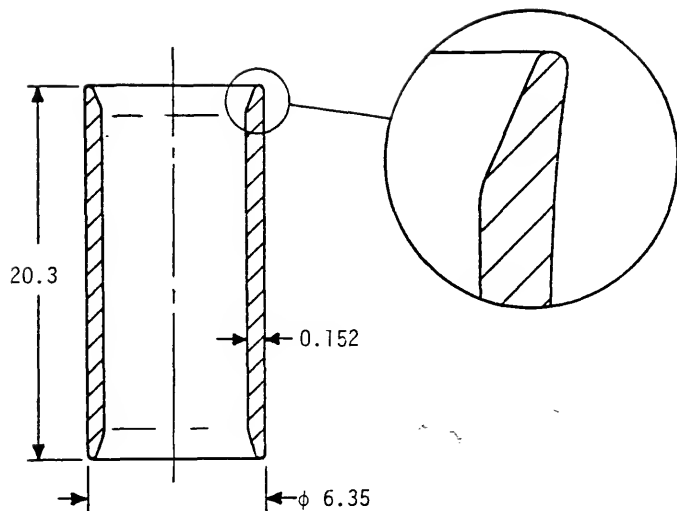
98

Figure E-1.   Dimensions of 304 stainless steel capsule used to contain sample, manganin gage and fluid.   Dimensions in mm.
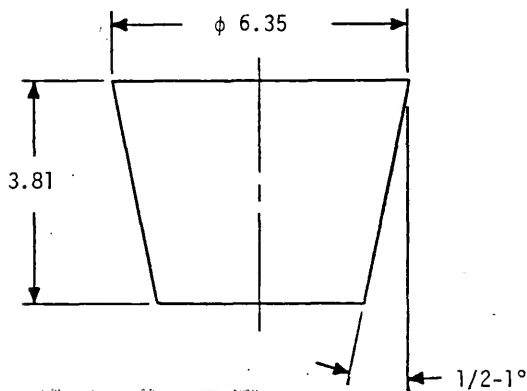

Figure E-2.   Configuration of polyethylene end plug.   Dimensions in mm.

successful, it was not possible to perform electrical tests at high voltages. It was concluded that pyrophyllite becomes conductive in high electric fields. Finally two leads made of No. 28 magnet wire were found to be successful at high pressures and up to 2000 V when tested in a cell similar to that shown in Figure 10.

It was necessary to feed six leads into the cell as follows: four for the two-terminal manganin cell resistance measurement and two for the test specimen. One of the manganin cell lead wires could have been connected to the specimen; however, the connection problems within the cell were more cumbersome than adding an additional lead.

Lead wire holes in the polyethylene were made by first manually drilling a pilot hole using a 0.18-mm-dia. drill. Lead wire holes were then drilled through the polyethylene using a No. 80 drill (0.343-mm dia.). Threading the wire through this hole required stripping 7 to 10 cm of insulation from the end of the enameled magnet wire. The bare wire was then sanded to a taper over a 3- to 6-cm length (using 400 and 600 grit emery paper) and threaded through a hole. Once the end protruded, it was pulled through with needle-nose pliers. If care was taken, the same wire could be used for several holes.

The hole configuration on both the top and lower side of the bottom plug is shown in Figure E-3. Drilling these holes was achieved by resting a fixture containing
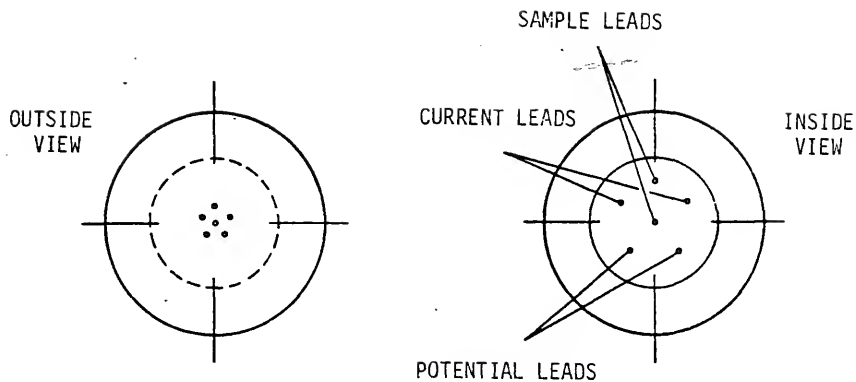
Figure E-3. Location of lead wire holes in end plug as viewed from the end on the outside of the capsule and the end on the inside of the capsule.
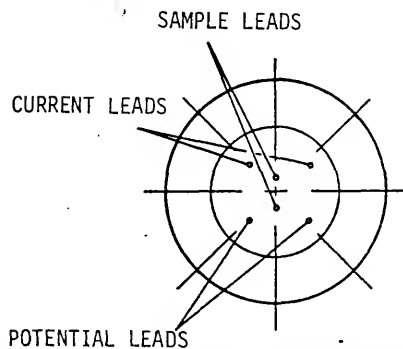

Figure E-4. A possible preferred lead wire location in end plug which has the advantage that the sample lead wires are positioned symmetrically on the plug.

the plug on an inclined plane at the appropriate angle to give the desired pattern. The pattern shown in Figure E-3 provided for lead wire separation within the cell and compaction of the lead wires at the point where they protruded and entered the vertex tetrahedron. The disadvantage of this configuration was that the manganin cell and sample were not centered in the cell. Perhaps a more desirable configuration is illustrated in Figure E-4.

The length of the lead wire protruding from the lower surface of the bottom plug was approximately 15 cm. A sketch of the completed bottom plug assembly is shown in Figure E-5. The current and potential leads going to each side of the manganin cell are continuous making it possible to strip a small portion of the insulation from the wires using a model F pencil blasting* unit (SiO_2 abrasive was used). A small amount of 65-35 Pb-Sn soft solder then was placed on this uninsulated area.

---

*SS White Co., New York, N. Y.

SAMPLE LEADS
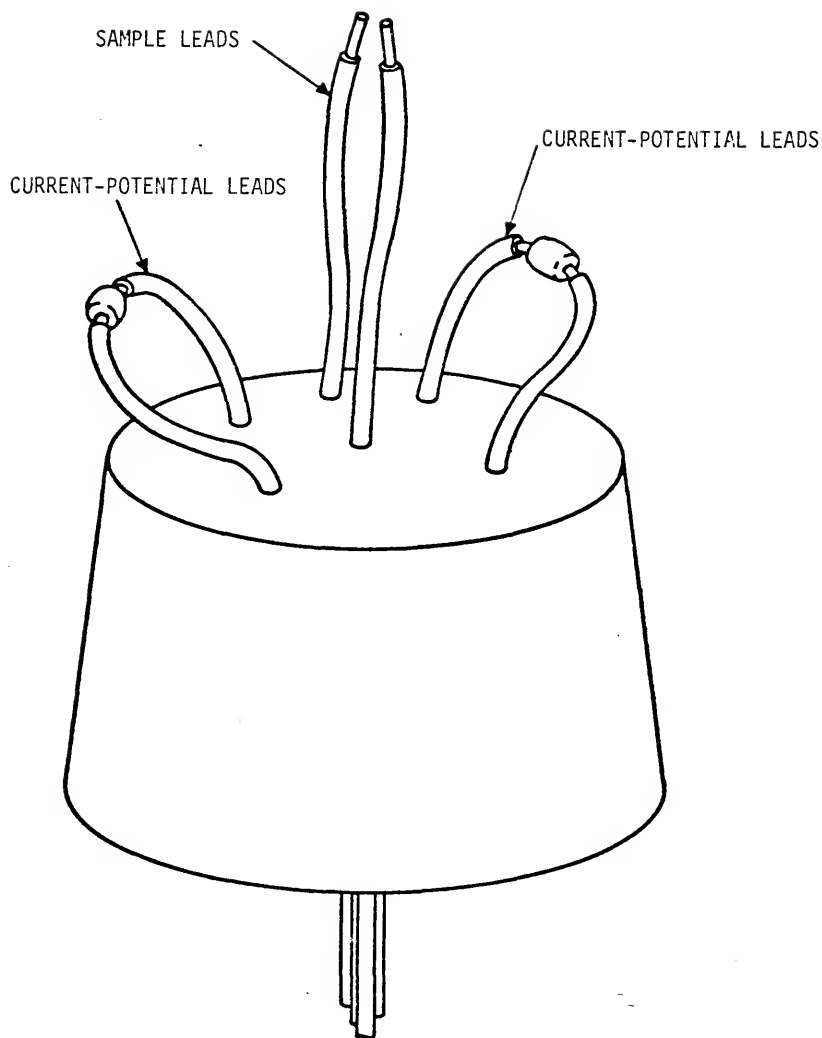
CURRENT-POTENTIAL LEADS

CURRENT-POTENTIAL LEADS

Figure E-5. The final configuration of the polyethylene bottom end
plug with lead wires in place. The current-potential
wires for four terminal resistance measurements are not
separate but are used as an integral feedthrough.

APPENDIX F

DIELECTRIC TEST FLUID

Because most fluids solidify above 2 GPa (43),
and only a limited number are available as high pressure
test media, Piermarini et al. (44) have examined the flu-
idity of several liquids and found that a 4 to 1 mixture
by volume of ethanol and methanol remained fluid to 10
GPa while a 1 to 1 mixture by volume of pentane and iso-
pentane was fluid to at least 7 GPa.

Both fluid mixtures were examined; however, the
alcohol mixture became conductive (apparently due to
moisture pickup). Thus, pentane grade 1501* and isopen-
tane grade 2370* mixture was the test fluid selected for
use. Because of their excellent dielectric properties, it
would have been desirable to use fluorocarbon liquids;
however, fluidity data with pressure were not found.

During the initial phases of the program in which
a variety of problems were encountered, extreme care was
taken to insure against moisture contamination, i.e.,
assembly of the test cell was performed in a dry room having

---

*Fisher Scientific Co., Fair Lawn, N. J.

a moisture content of less than 16 ppm or in a dry box.
However, as the program progressed, it was found that these
precautions were not necessary and it was possible to
assemble and add fluid in the 50 to 60% humidity test site
environment.

APPENDIX G

ASSEMBLY OF CAPSULE AND TEST CELL

The manganin cell and test specimen were mounted in
the capsule by soft soldering their leads to the magnet
wire leads protruding through the bottom polyethylene plug.
The recommended method of joining manganin is by hard sol-
dering (45, p. 124). This technique was attempted for the
manganin wire used in these studies, but difficulties were
encountered because of the small sizes involved. Resistance
welding was also attempted and was partially successful,
but the weld tabs occupied an excessive amount of space
in the capsule. Soft soldering appeared to be the only
alternative. By using an ammonium chloride base flux and
by wrapping the copper magnet wire several times with the
manganin wire, contact resistance was minimized.

The procedure used for test cell assembly was as
follows:

1. The solder nodule deposited on the current-
    potential lead was flattened with smooth-faced
    pliers and a 0.71-mm-dia. hole was manually
    drilled through the flattened region.

2. The manganin cell was positioned on the end plug by feeding the two specimen lead wires through the holes provided. The manganin leads were wound around each of the current-potential leads by threading through the 0.71-mm-dia. hole and wrapping three to four times as shown in Figure G-1.

3. The solder was reflowed. A drop of ammonium chloride solder flux was used to aid in wetting the manganin. The excess manganin wire lead was cut off.

4. After ultrasonic cleaning in Freon TF ® * and acetone, the current-potential leads were drawn tight against the polyethylene plug.

5. The enamel insulation was removed from magnet wire sample leads. The uninsulated portions of the leads were cut to 3-5 mm in length and tinned with an 80% In-20% Pb solder using an ammonium chloride base flux. Gold lead wires, such as those ball-bonded to the ferroelectric test specimen, are less susceptible to embrittlement with indium-based (rather than tin-based) solders.

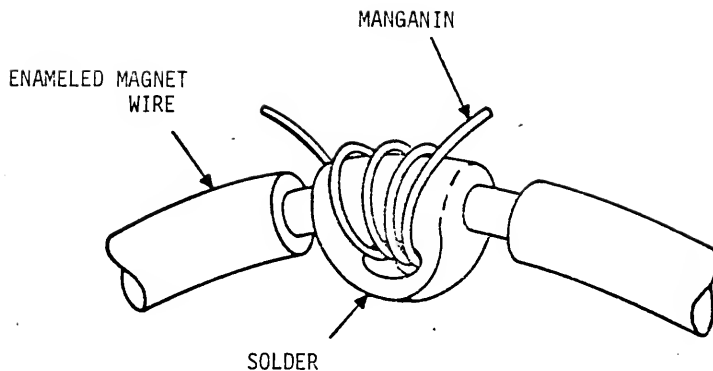*E. I. duPont de Nemours & Co., Wilmington, Del.

Figure G-1.   Attachment of manganin wire to current-potential lead
wire.   After positioning the manganin wire in place, the
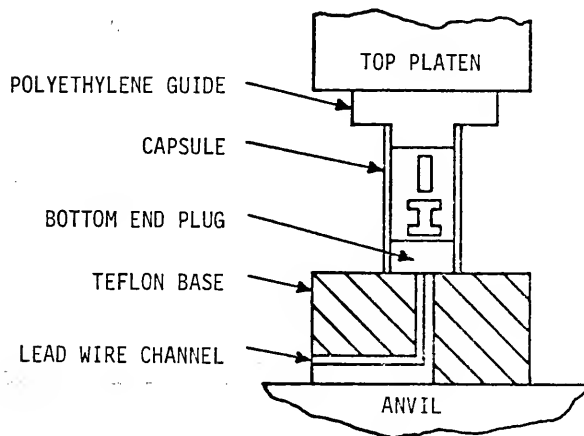solder was reflowed.

Figure G-2.   Technique used to install end plug in capsule.   After
positioning the assembly in an arbor press, the end
cap was forced into place.

6. The leads on the test specimen were cut to a length of 5-7 mm and attached to the plug lead wires by reflowing the In-Pb solder.

7. The assembly was ultrasonically cleaned in Freon TF ®, ethanol and acetone. After vacuum oven drying, the lead wires were drawn through a plug to reduce slack and position the test sample.

8. The lower plug was placed in the capsule. This was accomplished with an arbor press as shown in Figure G-2.

9. The capsule was filled with the dielectric fluid and the top plug was inserted using a technique similar to that shown in Figure G-2. The end plugs were flush with the ends of the capsule.

10. The capsule was placed in the pyrophyllite tetrahedron and the lead wires were fed through the hole in the vertex tetrahedron. A room temperature curing epoxy adhesive was applied to the mating surfaces. The adhesive was polymerized under pressure by curing while mounted in an arbor press.

11. The electrical leads extruding from the assembly were cut into 15-cm lengths and the ends stripped of enamel and tinned. A 12-cm length

of small diameter shrinkable tubing was
slipped over the leads and drawn tight against
the tetrahedron. Lengths of #20 Teflon ®
insulated stranded copper electrical wire
1.5-cm long were soft soldered to the manganin
gage leads from the tetrahedron. The center
lead of two 1.5-m-long coaxial cables (RG174)
were soldered to the ferroelectric sample leads.
The free end of these leads had BNC connectors
for attachment to the high voltage power supply
and the capacitance bridge. Shrink tubing was
used about each of the six connections.

APPENDIX H

CALIBRATION OF THE MANGANIN GAGE AND HEISE GAGE

At pressures up to 1.0 GPa, the resistivity of manganin varies almost linearly with pressure although at higher pressures nonlinear effects are encountered. Decker et al. (42, p. 817) have examined the first-, second- and third-order fit of the pressure-resistance relationship and concluded that the second-order equation was the most representative. Their recommended relationship (42, p. 820) which was based on the Hg_{S-L} (at 20.36° C) and Bi_{I-II} (at 23.5° C) transition is as follows:

$$p = 41.761 \ (\Delta R/R) + 33.82 \ (\Delta R/R)^2 \qquad (H-1)$$

where p is pressure in GPa.

Calibration of the manganin wire used for this study was performed by examining its response in a gas (dry nitrogen) isostatic press as well as its response at the Bi_{I-II} transition using the tetrahedral press. For the gas isostatic press, calibration was performed using a BLH 100,000 psi (0.6895 GPa) pressure transducer which was accurate to ± 0.15%. This transducer is calibrated on a

regular basis using a dead weight procedure. The same manganin gage was used for all calibration tests. This gage as well as all others used in these tests was seasoned several times prior to use by heating to 140° C in a vacuum oven for 48 hours or more and then quenching in liquid nitrogen.

Four tests on the isostatic press were made for calibration purposes. These were performed slowly to reduce thermal effects. Approximately 20 data points were taken from 0 to 0.68 GPa. The ambient temperature was approximately 23.5° C.

An uncertainty involved the zero pressure resistance reading which drifted slightly on both the isostatic press and the tetrahedral anvil device. Once pressure was applied, the readings stabilized. For the isostatic press, to obtain the zero pressure resistance value, a second-order fit of pressure versus resistance was determined. The result was extrapolated to zero and used to find $\Delta R/R$ for each of the four runs at a pressure of 0.6895 GPa with R calculated from the second-order fit of the data. The average value of $\Delta R/R$ was 0.01629.

The Bi_{I-II} transition pressure recommended for use by Decker et al. (42, p. 820) at 23.5° C is 2.5608 GPa. This value was originally reported by Heydemann (46) who examined the transition while the pressure was both increasing and decreasing. These values do not coincide;

the hysteresis between them is called the region of indifference. The value selected was an average between the two.

The most common technique of obtaining fixed point calibration data measures resistivity changes of the material at the transition. However, based on a suggestion by A. A. Giardini (47), it was decided to make use of the Bi_{I-II} volume change at the transition. This was possible since $\Delta V/V$ was significant enough to affect the pressure within the test cell which could in turn be detected with the manganin gage. The first successful test used a bismuth sample (grade B319)* weighing 0.19 gm. A slight discontinuity in pressure at the Bi_{I-II} transition was observed. A sample weighing 0.427 gm was used on the next two tests. The configuration of the calibration test cell is shown in Figure H-1. After each test, the cell was opened and the Bi sample examined. It was not distorted, indicating that the pressure environment about the bismuth was truly hydrostatic. Since the bismuth used was in granular form, a solid rod was made by melting a small amount in a 4-mm I.D. closed-end fused quartz tube. Although bismuth expands during solidification, the coefficient of expansion of bismuth is substantially greater than fused quartz and the sample usually fell out at ambient temperature.

---

*Fisher Scientific Co., Fair Lawn, N. J.

POLYETHYLENE END PLUG

WIRE USED TO HOLD BISMUTH
IN TOP OF CELL

HOLE

BISMUTH

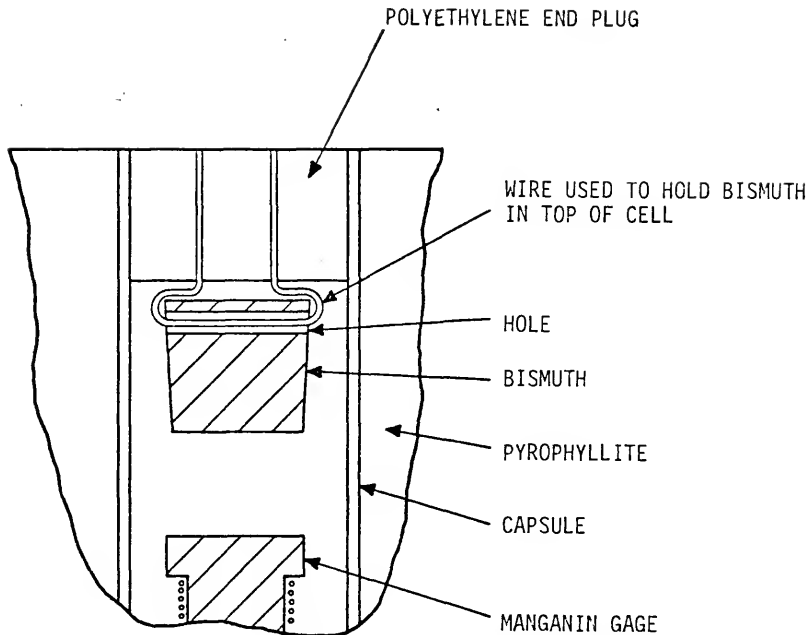PYROPHYLLITE

CAPSULE

MANGANIN GAGE

Figure H-1.   Cross-section of test cell configuration used to cali-
brate manganin gage using bismuth. The bismuth is
tapered to allow the test cell to collapse and not
interfere. The bismuth is held to the top end plug so
that it will not contact the manganin gage.

For increasing pressure the results for test Number 3 (see Figure H-2) show both the Bi_{I-II} transition as well as the 2.705 GPa Bi_{II-III} transition (48, p. 304). The magnitude of the Bi_{II-III} transition was surprising since the Bi_{II-III} resistance change noted in the open literature appears significantly smaller than the Bi_{I-II} transition.

For decreasing pressure the resistance change at the Bi_{I-II} transition is shown in Figure H-3. The region of indifference was approximately 0.1 GPa. For calibration purposes, an average ΔR/R based on the values at points A and B in Figure H-2 and H-3 were selected. As with data from the isostatic press, the zero resistance results were determined by fitting the gage resistance versus Heise gage reading to a second-order equation and extrapolating to zero. Pressure was applied at a slow rate to allow the temperature to reach equilibrium between each measurement.

For the 2.5608 GPa Bi_{I-II} transition, ΔR/R was 0.057501. This, along with the isostatic press ΔR/R value of 0.01629 at 0.6895 GPa resulted in the following calibration equation:

$$p = 41.623\ (\Delta R/R) + 43.892\ (\Delta R/R)^2 \qquad (H-2)$$
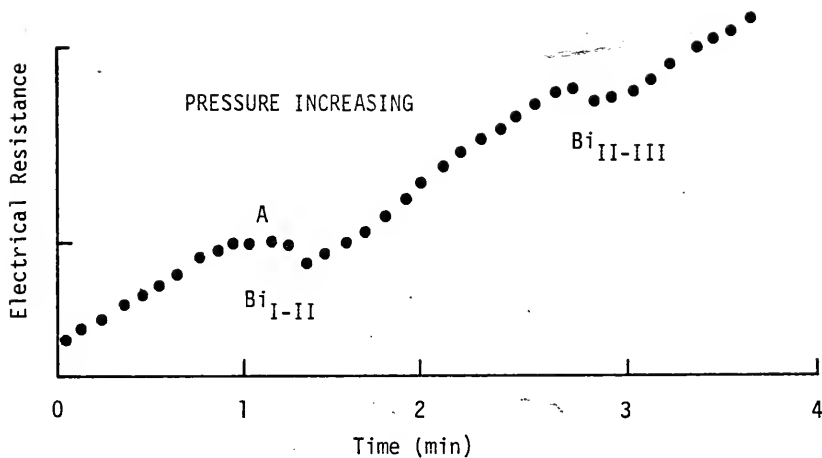
where p is pressure in GPa.

Figure H-2. Variation of manganin gage electrical resistance during pressurization cycle. At the transition a volume change results in a pressure change within the cell. A measurement was made every 5 sec.
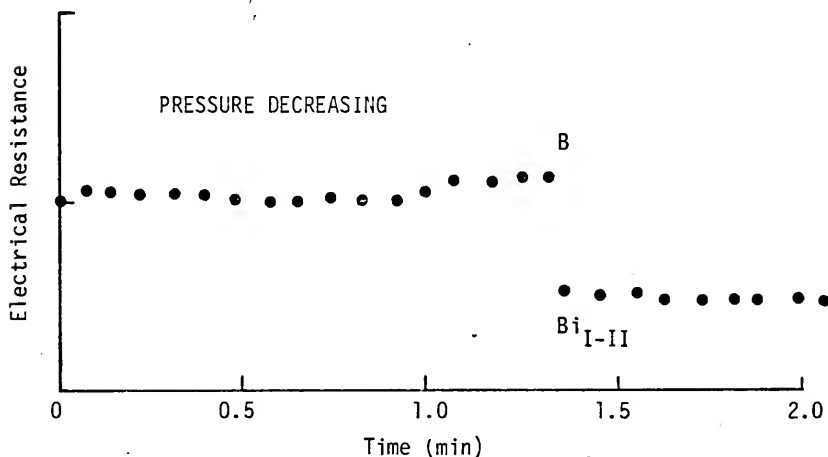

Figure H-3. Variation of manganin gage electrical resistance during depressurization cycle. The Bi_{I-II} phase change caused a change in pressure in the test cell because of its volume change.

This equation agrees with Equation H-1 within 1% up to the Bi_{I-II} transition. More detailed information concerning the Bi_{I-II} transition hysteresis is described by Zeto et al. (49).

While calibrating the manganin gage it was also possible to determine the test cell pressure versus the Heise gage pressure reading on the tetrahedral anvil press control panel. This information was needed for the data reduction of a series of early tests in which defective manganin wire was used. The accuracy of the calibration is questionable because the pressure transmitted to the sample is dependent on numerous factors such as the sample geometry and the rate at which pressure is applied. For instance, if pressure is applied rapidly, then higher pressures can be reached for a given Heise gage reading than at lower application rates. As mentioned previously, pressure was applied slowly for these tests. The resulting relationships are as follows:

for 0 to 1000 psi on the Heise gage,

$$p = 1.203 \times 10^{-3} (X) - 2.97 \times 10^{-7} (X)^2 \qquad (H-3)$$

and for 1000 to 5000 psi on the Heise gage,

$$p = 0.056 + 9.18 \times 10^{-4} (X) - 6.73 \times 10^{-8} (X)^2$$

(H-4)

where X is the Heise gage reading in psi and p is pressure in GPa.

BIBLIOGRAPHY

1. F. W. Nielson, Sandia Memo #230B-56-51 (Sandia Corp., Albuquerque, N. M., Nov. 1956).

2. E. Sawaguchi, J. Phys. Soc. Japan $\underline{8}$, 615 (1953).

3. D. A. Berlincourt, Annual Progress Report on Piezo-electric Materials, Sandia Labs P. O. #51-6542 (Sandia Corp., Albuquerque, N. M., March 1960).

4. G. W. Anderson, Sandia Memo #224-57-51 (Sandia Corp., Albuquerque, N. M., Aug. 1957).

5. P. C. Lysne and C. M. Percival, J. Appl. Phys. $\underline{46}$, 1519 (1975).

6. P. J. Chen and M. C. McCarthy, Int. J. Solids Structures $\underline{10}$, 1229 (1974).

7. P. C. Lysne, Private Communication.

8. V. V. Danial, Dielectric Relaxation (Academic Press, New York, 1967).

9. C. B. Sawyer and C. H. Tower, Phy. Rev. $\underline{35}$, 269 (1930).

10. G. A. Samara, Phys. Rev. $\underline{151}$, 378 (1966).

11. D. A. Berlincourt, IEEE Trans. Solids and Ultrasonics SU-15, 89 (1968).

12. C. Kittel, Phys. Rev. $\underline{82}$, 729 (1951).

13. B. Jaffe, Proc. IEEE, $\underline{61}$, 1264 (1961).

14. F. Jona and G. Shirane, Ferroelectric Crystals (Macmillan Co., New York, 1962).

15. H. M. Barnett, J. Appl. Phys. $\underline{33}$, 1606 (1962).

16. S. Roberts, J. Am. Ceram. Soc. $\underline{33}$, 66 (1950).

17. B. Jaffe, W. R. Cook, and H. Jaffe, <u>Piezoelectric Ceramics</u> (Academic Press, New York, 1971).

18. D. A. Berlincourt and H. H. A. Krueger, Annual Progress Report on Piezoelectric Materials, Sandia P. O. #51-9689-A (Sandia Corp., Albuquerque, N. M., April 1963).

19. R. H. Dungan, H. M. Barnett, and A. H. Stark, J. Am. Ceram. Soc. <u>45</u>, 382 (1962).

20. M. Torccaz, L. Eyraud, Y. Fetiveau, P. Gonnard, and J. Paletto, CR Acad. Sciences Paris t 275, Serie B 597 (1972).

21. G. A. Samara, <u>Advances in High Pressure Research</u>, R. S. Bradley, Ed. (Academic Press, Inc., New York, 1969).

22. G. A. Samara, Ferroelectrics <u>2</u>, 277 (1971).

23. G. A. Samara, Phys. Rev. <u>151</u>, 378 (1966).

24. G. A. Samara and A. A. Giardini, Phys. Rev. <u>140</u>, A954 (1965).

25. I. N. Polandov, V. I. Kalinin, N. P. Kachalov, and G. P. Isaev, Vestnik Moskovskogo Universitita, Khimiya, <u>30</u>, 244 (1975).

26. P. Gonnard, Y. Fetiveau, F. Bauer, and L. Eyraud, C. R. Acad. Sc. Paris t 275, Serie B 633 (1972).

27. W. J. Halpin, J. Appl. Phys. <u>37</u>, 153 (1966).

28. C. E. Reynolds and G. E. Seay, J. Appl. Phys. <u>32</u>, 1401 (1961).

29. C. E. Reynolds and G. E. Seay, J. Appl. Phys. <u>33</u>, 2234 (1962).

30. D. G. Doran, F. E. Materials Under Shock, SRl Project No. PGD-3483 (Stanford Res. Inst., Menlo Park, Calif., Nov. 1962).

31. D. G. Doran, J. Appl. Phys. <u>39</u>, 40 (1968).

32. R. K. Linde, J. Appl. Phys. <u>38</u>, 4839 (1967).

33. P. C. Lysne, R. A. Graham, L. C. Bartel, and G. A. Samara, "Shock Wave Induced Phase Transformation: A Review of the Field," Report No. SC-TM-710907 (Sandia Corp., Albuquerque, N. M., 1971).

34. J. W. Nunziato and E. K. Walsh, Arch. Rational Mech. Anal. 64, 299 (1977).

35. M. A. Goodman and S. C. Cowin, Arch. Rational Mech. Anal. 44, 249 (1972).

36. H. T. Hall, Rev. of Sci. Inst. 29, 267 (1958).

37. E. C. Lloyd, U. O. Hutton, and D. P. Johnson, J. Res. N. B. S. C Eng. and Inst. 63C, 59 (1959).

38. M. D. Banus and S. D. Nye, Rev. of Sci. Inst. 35, 1319 (1964).

39. H. T. Hall, Progress in Very High Pressure Research, F. P. Bundy, W. R. Hibbard, and H. M. Strong, Eds. (John Wiley and Sons, New York, 1961).

40. J. Lees, Nature 203, 965 (1964).

41. D. L. Decker, J. D. Jorgensen, and R. W. Young, High Temp. - High Press. 7, 331 (1975).

42. D. L. Decker, W. A. Bassett, L. Merrill, H. T. Hall, and J. D. Barnett, J. Phys. Chem. Ref. Data 1, 773 (1972).

43. P. W. Bridgman, Collected Experimental Papers (Harvard U. Press, Cambridge, Mass., 1964).

44. G. J. Piermarini, S. Block, and J. D. Barnett, J. Appl. Phys. 44, 5377 (1973).

45. S. E. Babb, Jr., High Pressure Measurements, A. A. Giardini and E. C. Lloyd, Eds. (Butterworths, Washington, 1963).

46. P. L. M. Heydemann, J. Basic Eng. 89, 551 (1967).

47. A. A. Giardini, Private Communication.

48. G. C. Kennedy and P. N. LaMari, Progress in Very High Pressure Research, F. P. Bundy, W. R. Hibbard, and H. M. Strong, Eds. (John Wiley and Sons, Inc., New York, 1961).

49. R. J. Zeto, H. B. Vanfleet, E. Hryckowian, and C. D. Bosco, N. B. S. Bull #326 (N. B. S., Washington, D. C., 1968).

BIOGRAPHICAL SKETCH

Richard Kent Spears was born and raised in the northeastern Colorado town of Brush. Following his graduation from Brush High School in 1955, he studied Metallurgical Engineering at the Colorado School of Mines in Golden where he was awarded a B. S. degree in 1959. Following graduation, while working for the Martin Company in Denver, he enrolled in the graduate program at the University of Denver and received an M. S. degree in Metallurgical Engineering in 1964. In 1966 he joined the General Electric Company, Neutron Devices Department, St. Petersburg, Florida, and in 1967 he enrolled at the University of South Florida in Tampa, hoping to attain a Ph. D. even though at that time the program was not approved at that institution. When it became evident that an Engineering Ph. D. program would not be granted for a considerable time, he enrolled in the Department of Engineering Sciences at the University of Florida in Gainesville in 1974. Since then, he has been working toward a Ph. D. degree in Engineering Mechanics which is to be awarded in August 1977. During this time he continued his employment with the General Electric Company.

I certify that I have read this study and that in my opinion it conforms to acceptable standards of scholarly presentation and is fully adequate, in scope and quality, as a dissertation for the degree of Doctor of Philosophy.

E. K. Walsh, Chairman
Professor of Engineering
    Sciences

I certify that I have read this study and that in my opinion it conforms to acceptable standards of scholarly presentation and is fully adequate, in scope and quality, as a dissertation for the degree of Doctor of Philosophy.

M. A. Eisenberg
Professor of Engineering
    Sciences

I certify that I have read this study and that in my opinion it conforms to acceptable standards of scholarly presentation and is fully adequate, in scope and quality, as a dissertation for the degree of Doctor of Philosophy.

C. S. Hartley
Professor of Materials
    Science

I certify that I have read this study and that in my opinion it conforms to acceptable standards of scholarly presentation and is fully adequate, in scope and quality, as a dissertation for the degree of Doctor of Philosophy.
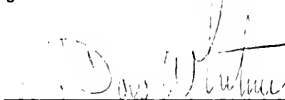
S. Y. Lu
Associate Professor of
    Engineering Sciences

I certify that I have read this study and that in my opinion it conforms to acceptable standards of scholarly presentation and is fully adequate, in scope and quality, as a dissertation for the degree of Doctor of Philosophy.

L. E. Malvern
Professor of Engineering
    Sciences

I certify that I have read this study and that in my opinion it conforms to acceptable standards of scholarly presentation and is fully adequate, in scope and quality, as a dissertation for the degree of Doctor of Philosophy.

E. D. Whitney
Professor of Materials
    Science

This dissertation was submitted to the Graduate Faculty of the Department of Engineering Sciences in the College of Engineering and to the Graduate Council, and was accepted as partial fulfillment of the requirements for the degree of Doctor of Philosophy.

August, 1977

Dean, College of Engineering

Dean, Graduate School